A New Cross-Space Total Variation Regularization Model for Color Image Restoration with Quaternion Blur Operator

Zhigang Jia, Yuelian Xiang, Meixiang Zhao, Tingting Wu, Michael K. Ng

Abstract—The cross-channel deblurring problem in color image processing is difficult to solve due to the complex coupling and structural blurring of color pixels. Until now, there are few efficient algorithms that can reduce color artifacts in deblurring process. To solve this challenging problem, we present a novel cross-space total variation (CSTV) regularization model for color image deblurring by introducing a quaternion blur operator and a cross-color space regularization functional. The existence and uniqueness of the solution are proved and a new L-curve method is proposed to find a balance of regularization terms on different color spaces. The Euler-Lagrange equation is derived to show that CSTV has taken into account the coupling of all color channels and the local smoothing within each color channel. A quaternion operator splitting method is firstly proposed to enhance the ability of color artifacts reduction of the CSTV regularization model. This strategy also applies to the well-known color deblurring models. Numerical experiments on color image databases illustrate the efficiency and effectiveness of the new model and algorithms. The color images restored by them successfully maintain the color and spatial information and are of higher quality in terms of PSNR, SSIM, MSE and CIEde2000 than the restorations of the-state-of-the-art methods.

Index Terms—Color image restoration; Cross-channel deblurring; Cross-space total variation; Quaternion operator splitting; Saturation value total variation.

I. INTRODUCTION

Zhigang Jia is with the School of Mathematics and Statistics & RIMS, Jiangsu Normal University, Xuzhou 221116, P.R. China (e-mail: zhgjia@jsnu.edu.cn).

Yuelian Xiang is with the School of Mathematics and Statistics, Jiangsu Normal University, Xuzhou 221116, P.R. China and also with the General Education School, Wuhan Vocational College of Software and Engineering, Wuhan 430205, P.R. China (e-mail: yuelianx@126.com).

Meixiang Zhao is with the School of Mathematics and Statistics, Jiangsu Normal University, Xuzhou 221116, P.R. China (e-mail: zhaomeixiang2008@126.com).

Tingting Wu is with the School of Science, Nanjing University of Posts and Telecommunications, Nanjing 210003, P.R. China (e-mail: wutt@njupt.edu.cn).

Michael K. Ng is with the Department of Mathematics, Hong Kong Baptist University, Hong Kong (e-mail: michael-ng@hkbu.edu.hk).

Cross-channel deblurring is one of the most important topics in color image processing. It is difficult to solve due to the complex coupling and structural blurring of color pixels that are difficult to characterize. The classic and advanced color image total variation (TV) regularization restoration models, consisting of regularization and fidelity terms, have made outstanding contributions to denoising and deblurring. However, their innovation is focused on the improvement of TV regularization term on one color space and there is still a lack of efficient algorithms that can reduce color artifacts. A long-overlooked, but very important, requirement to develop advanced models is to define color TV regularization functional on different color spaces and develop algorithm that preserves the coupling of color pixels. In this paper, we present a novel cross-space TV (CSTV) regularization model for color image restoration that achieves such requirement. Moreover, we develop a general quaternion operator splitting algorithm to enhance the ability of reducing color artifacts of color image deblurring models.

A groundbreaking color image regularization is the (global) channel coupling color TV [1], followed by a local version [2]. These two regularization functionals couple red (R), green (G) and blue (B) channels by different norms of TVs on three channels, that is, norms of vectorial TV of color image in the RGB color space. A general framework, called collaborative TV [6], incorporates various norms along different dimensions to provide a comprehensive approach to regularization and the considered norms includes nuclear, Frobenius and spectral norms. Recently, Duan et al. [5] proposed a new Beltrami regularization model for color image denoising and an efficient and robust operator splitting method, with regarding color images as manifolds embedded in a five dimensional spatial-chromatic space. And a new color elastica model is developed in [23], [24] by using the Polyakov action and a Laplace–Beltrami operator on color channels. These beautiful regularization functionals greatly enriched color image models based on vector representation in one color space.

To find more efficient manners of coupling, various studies explore color space transformation methods to generate regularization functionals on new color space. The chrominance, luminance, or R/B component was formed through a weighted linear combination of the R, G and B channels of the color image in [3]. This process is also represented as $\sum_k TV(u_k \circ \psi)$ in [6], where ψ is an orthonormal transform to describe the color space transformation. Besides, the human eye is highly sensitive to changes in the opponent

color channel. In [25], the opponent transform is employed to transform the RGB color space into the opponent space and the decomposition of the coupling of color channels is allowed. Recently, a novel saturation-value TV (SVTV) regularization model is introduced in [19] based on quaternion representation of color images and the existence and uniqueness of the solution are proved. Such SVTV regularization functional successfully reflects the physical principle of the human visual system and considers the coupling of color channels. So SVTV reconstructs color images of high quality and with slight color artifacts. In these years, the SVTV regularization functional has been combined with other methods to handle other image processing tasks and the new models achieve at a high level on numerical performance; see [15], [31]–[33] for instance. Above models consider color image restoration in a single color space and their regularization functionals have been well known for their prior on color edges.

Unlike the successful improvement of regularization terms, the development of fidelity terms of color image restoration models has been hindered for a long time by the difficulty of characterizing complex coupling and structured blur of color pixels and the hardness to eliminate color artifacts. A new understanding of the blurring process is in need. Recall that a general color image degradation model (see [9], [10], [12] for instance) is

$$z(x,y) = \hat{K} \star u(x,y) + n(x,y), \tag{1}$$

where $z(x,y), \hat{K}, u(x,y), n(x,y)$ denote degraded color image, blur operator, original color image and additive noise, respectively, and (x,y) refers to their pixel coordinates. Conventionally, the blur operator $\hat{K}$ is a three-by-three block matrix consisting of several two-dimensional convolution operators [12] and the fidelity functionals are defined by different norms of $\hat{K} \star u(x,y) - z(x,y)$. In order to make progress, we use quaternions to represent color pixels and introduce a novel quaternion convolution operator $\mathbf{Q}$ (defined in Section III-A) to characterize the cross-channel blurring process. This blur operator $\mathbf{Q}$ depicts the mutual artifacts between color channels. It can be seen as a splitting factor of $\hat{K}$ and is used to improve the fidelity term.

To the best of our knowledge, there are still no cross-color space mathematical model with strict proof of existence and uniqueness of the solution for color image cross-channel deburring problem. In this paper, we present a novel color image restoration model to solve the cross-channel deblurring problem and theoretically analyze its solvability. The contribution is in three aspects:

- A CSTV regularization model is presented for color image restoration by introducing a novel quaternion blur operator and a new regularization functional. The CSTV regularization functional is defined on different color spaces and preserves the coupling of color pixels in the deblurring process. This generalizes the well-known TV regularization terms from one color space to two or more color spaces.
- A new quaternion operator splitting algorithm is developed to enhance the ability of reducing color artifacts in deblurring process of the proposed CSTV regularization

model. This quaternion operator splitting algorithm is universal and can be applied to improve classical color image deblurring models.
- The newly proposed models and algorithms are applied to solve the cross-channel deblurring problems of natural color images. Their efficiency and superiority are indicated by numerical results in terms of visual, PSNR, SSIM, MSE and CIEde2000 criteria. These numerical results support the assertion that the proposed new methods can better preserve the color fidelity and texture.

This paper is organized as follows. In Section II, we recall preliminary information about quaternions and color TV regularization functionals. In Section III, we propose a novel CSTV regularization model for color image restoration and the corresponding existence and uniqueness theory of the solution. In Section IV, we present an effective quaternion operator splitting algorithm to solve the proposed CSTV regularization model. In Section V, we demonstrate numerical examples to illustrate the superiority of the proposed methods. In Section VI, we present concluding remarks.

II. PRELIMINARIES

In this section, we shortly review quaternions and the existing TV regularization functionals for color image processing.

Let $\mathbb{Q} = \{a_0 + a_1\mathbf{i} + a_2\mathbf{j} + a_3\mathbf{k} \mid a_0, a_1, a_2, a_3 \in \mathbb{R}\}$ denote the quaternion skew-field, $\mathbb{Q}^n$ the set of n-dimensional quaternion vectors, and $\mathbb{Q}^{m \times n}$ the set of $m \times n$ quaternion matrices [13], where three imaginary units $\mathbf{i}, \mathbf{j}, \mathbf{k}$ satisfy

$$\mathbf{i}^2 = \mathbf{j}^2 = \mathbf{k}^2 = \mathbf{ijk} = -1.$$

For a quaternion $\mathbf{a} = a_0 + a_1\mathbf{i} + a_2\mathbf{j} + a_3\mathbf{k}$, a_0 is called real part and a_1, a_2, a_3 are called three imaginary parts. Pure quaternion is nonzero quaternion with zero real part. The conjugate and modulus of $\mathbf{a}$ are defined by $\bar{\mathbf{a}} = a_0 - a_1\mathbf{i} - a_2\mathbf{j} - a_3\mathbf{k}$ and $|\mathbf{a}| = \sqrt{\bar{\mathbf{a}}\mathbf{a}} = \sqrt{a_0^2 + a_1^2 + a_2^2 + a_3^2}$, respectively. Every nonzero quaternion is invertible and its unique inverse is defined by $\mathbf{a}^{-1} = \bar{\mathbf{a}}/|\mathbf{a}|^2$. The conjugate transpose of quaternion vector $\mathbf{v} = v_0 + v_1\mathbf{i} + v_2\mathbf{j} + v_3\mathbf{k} \in \mathbb{Q}^n$ is defined as $\mathbf{v}^* = v_0^T - v_1^T\mathbf{i} - v_2^T\mathbf{j} - v_3^T\mathbf{k}$, where $v_0, v_1, v_2, v_3 \in \mathbb{R}^n$ and $\cdot^T$ denotes the transpose operator. Similarly, the conjugate transpose of quaternion matrix $\mathbf{A} = A_0 + A_1\mathbf{i} + A_2\mathbf{j} + A_3\mathbf{k} \in \mathbb{Q}^{m \times n}$ is defined as $\mathbf{A}^* = A_0^T - A_1^T\mathbf{i} - A_2^T\mathbf{j} - A_3^T\mathbf{k}$, where $A_0, A_1, A_2, A_3 \in \mathbb{R}^{m \times n}$. The inner product of two quaternion vectors, $\mathbf{u} = [\mathbf{u}_i]$, $\mathbf{v} = [\mathbf{v}_i] \in \mathbb{Q}^n$, is defined as $\langle \mathbf{u}, \mathbf{v} \rangle = \sum_{i=1}^n \mathbf{v}_i^* \mathbf{u}_i$. According to [18], we define a homeomorphic mapping $\Re$ from quaternion matrices, vectors, scalars or operators to structured real matrices or operators:

$$\Re(\mathbf{A}) = \begin{bmatrix} A_0 & -A_1 & -A_2 & -A_3 \\ A_1 & A_0 & -A_3 & A_2 \\ A_2 & A_3 & A_0 & -A_1 \\ A_3 & -A_2 & A_1 & A_0 \end{bmatrix}. \tag{2}$$

The inverse mapping of $\Re$ on the structured real matrices is defined by $\Re^{-1}(\Re(\mathbf{A})) = \mathbf{A}$. Let $\Re_c(\mathbf{A})$ denote the first column of $\Re(\mathbf{A})$. The inverse mapping of $\Re_c$ is similarly defined by $\Re_c^{-1}(\Re_c(\mathbf{A})) = \mathbf{A}$.

Now we introduce the measurement of quaternion vectors and matrices. The absolute of quaternion vector $\mathbf{v} = [\mathbf{v}_i] \in \mathbb{Q}^n$

is $|\mathbf{v}| = [|\mathbf{v}_i|] \in \mathbb{R}^n$. Similarly, the absolute of quaternion matrix $\mathbf{A} = [\mathbf{a}_{ij}] \in \mathbb{Q}^{m \times n}$ is $|\mathbf{A}| = [|\mathbf{a}_{ij}|] \in \mathbb{R}^{m \times n}$. From [16], we know that quaternion vector (or matrix) norms are functions from quaternion vectors (or matrices) to nonnegative real numbers.

Definition 1. *Let $p \geq 1$. The p-norm of $\mathbf{v} \in \mathbb{Q}^n$ is $\|\mathbf{v}\|_p = \left(\sum_{i=1}^{n} |\mathbf{v}_i|^p \right)^{\frac{1}{p}}$. The p-norm and F-norm of $\mathbf{A} \in \mathbb{Q}^{m \times n}$ are*

$$\|\mathbf{A}\|_p = \max_{\mathbf{x} \in \mathbb{Q}^n / \{0\}} \frac{\|\mathbf{A}\mathbf{x}\|_p}{\|\mathbf{x}\|_p}, \ \|\mathbf{A}\|_F = \left(\sum_{i=1}^{m} \sum_{j=1}^{n} |\mathbf{a}_{ij}|^2 \right)^{\frac{1}{2}}.$$

From Definition 1, one can easily derive that $\|\mathbf{v}\|_2 = \|\Re_c(\mathbf{v})\|_2 = \frac{1}{2}\|\Re(\mathbf{v})\|_2$, $\|\mathbf{A}\|_2 = \|\Re(\mathbf{A})\|_2$ and $\|\mathbf{A}\|_F = \|\Re_c(\mathbf{A})\|_F = \frac{1}{2}\|\Re(\mathbf{A})\|_F$.

Next, we give a brief description of the SVTV regularization functional [19]. A pure imaginary quaternion function

$$\mathbf{u}(x, y) = u_1(x, y)\mathbf{i} + u_2(x, y)\mathbf{j} + u_3(x, y)\mathbf{k} \quad (3)$$

was used to represent a color image in the RGB color space in [19], where (x, y) denotes the position of a color pixel in a given range Ω and three real bivariate functions $u_i(x, y)$ ($i = 1, 2, 3$) denote pixel values of R, G and B channels, respectively. For convenience, we define a new transformation map $\mathcal{T}$ as

$$\mathcal{T}(\mathbf{q}(x, y)) := q(x, y) = [q_1(x, y), q_2(x, y), q_3(x, y)]^T \quad (4)$$

for $\mathbf{q}(x, y) = q_0(x, y) + q_1(x, y)\mathbf{i} + q_2(x, y)\mathbf{j} + q_3(x, y)\mathbf{k}$. A real-valued version of SVTV was also given in [19], which makes it possible to handle by real calculations instead of quaternion calculations. For simplicity, let $\partial_{x/y}$ denote ∂_x or ∂_y. Define $\partial_{x/y}\mathbf{u}(x, y) = \partial_{x/y}u_1(x, y)\mathbf{i} + \partial_{x/y}u_2(x, y)\mathbf{j} + \partial_{x/y}u_3(x, y)\mathbf{k}$ and

$$C = \begin{bmatrix} 2 & -1 & -1 \\ -1 & 2 & -1 \\ -1 & -1 & 2 \end{bmatrix}. \quad (5)$$

Let $u(x, y) = \mathcal{T}(\mathbf{u}(x, y))$. The saturation and value components of color image $\mathbf{u}(x, y)$ are defined as

$$|\mathbf{u}(x, y)|_s = \frac{1}{3}\|Cu(x, y)\|_2, |\mathbf{u}(x, y)|_v = \frac{1}{\sqrt{3}}|\sum_{i=1}^{3} u_i(x, y)|. \quad (6)$$

The SVTV regularization functional is defined in [19] by

$$\begin{aligned} \text{SVTV}(\mathbf{u}(x, y)) = \int_\Omega & \sqrt{|\partial_x \mathbf{u}(x, y)|_s^2 + |\partial_y \mathbf{u}(x, y)|_s^2} \\ & + \alpha \sqrt{|\partial_x \mathbf{u}(x, y)|_v^2 + |\partial_y \mathbf{u}(x, y)|_v^2} dxdy, \end{aligned} \quad (7)$$

where α is a weighting parameter. This is exactly a functional of real functions $u_1(x, y)$, $u_2(x, y)$ and $u_3(x, y)$.

Before SVTV regularization functional, there are several well-known TV regularization functionals developed for color image in the RGB color space. For instance,

• Blomgren and Chan [1]:

$$\text{CTV}_1(u(x, y)) := \sqrt{\sum_{i=1}^{3} \left(\int_\Omega \|\nabla u_i(x, y)\|_2 \ dxdy \right)^2}. \quad (8)$$

• Bresson and Chan [2]:

$$\text{CTV}_2(u(x, y)) := \int_\Omega \sqrt{\sum_{k=1}^{3} \|\nabla u_i(x, y)\|_2^2} \ dxdy. \quad (9)$$

• Sapiro [29]:

$$\text{VTV}(u(x, y)) := \int_\Omega f(\lambda((\nabla u(x, y))^T \nabla u(x, y))) dxdy, \quad (10)$$

where $\lambda(\cdot)$ refers to eigenvalues and $f(\cdot)$ is a penalty function on eigenvalues. In the above equations, $\nabla = [\partial_x, \partial_y]^T$ represents the gradient operator. In [6], classic and advanced versions of vector TV regularization functionals are summarized into a classification called collaborative total variation (CTV) regularization functional. When applied to color images, they are all based on one color space. A new regularization on different color spaces will be firstly introduced in this paper.

III. Cross-space total variation regularization model for color image restoration

In this section, we present a novel color image restoration model to solve the cross-channel deblurring problem.

With the degradation model (1) in hand, we are concerned with a general framework for color image restoration model

$$\min_{\substack{\lambda \in \mathbb{R}^m \\ u(x,y) \in \mathbb{BV}(\Omega)}} J(u, \lambda) + F(u, z, \hat{K}), \quad (11)$$

where $\mathbb{R}^m$ denotes the m-dimensional real-valued vector space, $\mathbb{BV}(\Omega) = \{u(x, y) = [u_1(x, y), u_2(x, y), u_3(x, y)]^T \mid u_i(x, y) \in \text{BV}(\Omega), (x, y) \in \Omega\}$ and $\text{BV}(\Omega)$ is bounded variation space in a given region $\Omega \subseteq \mathbb{R}^2$. The functional $F(u, z, \hat{K})$ is a data fidelity term to control the distance between the targeted and observed color images under the blurring operator. The functional $J(u, \lambda)$ punishes the gradients of the targeted color image $u(x, y)$ in different color spaces and it is called a cross-color space regularization term with regularization parameters $\lambda = (\lambda_1, \lambda_2, \cdots, \lambda_m) \in \mathbb{R}^m$.

A. Fidelity functional with quaternion blur operator

The fidelity functional $F(u, z, \hat{K})$ aims to minimize the distance between the observed color image z and the original color image u after a blurring operation. In this subsection, we introduce a new characterization of blur process by quaternion operator, which leads to an algorithm to compute a solution without color artifacts. At first, we recall the cross-channel blur mechanism. The color image cross-channel blurring process is mathematically described as

$$\hat{u}(x, y) = \hat{K} \star u(x, y), \quad (12)$$

where

$$\hat{K} = W \odot K = [K_{ij}\omega_{ij}]_{3 \times 3},$$

$$K = \begin{bmatrix} K_{11} & K_{12} & K_{13} \\ K_{21} & K_{22} & K_{23} \\ K_{31} & K_{32} & K_{33} \end{bmatrix}, \ W = \begin{bmatrix} w_{11} & w_{12} & w_{13} \\ w_{21} & w_{22} & w_{23} \\ w_{31} & w_{32} & w_{33} \end{bmatrix}. \quad (13)$$

In formula (13), K_{ij}'s are real blur kernels, w_{ij}'s belong to the interval $[0, 1]$ with satisfying $\sum_{j=1}^{3} w_{ij} = 1$ for $i = 1, 2, 3$, and the symbol $\odot$ denotes the Hadamard product. Here, $\star$ denotes the two-dimensional convolution operator and the formula (12)

characterizes the blurring process $\hat{u}_i(x,y) = \sum_{j=1}^{3}(K_{ij}w_{ij}) \star u_j(x,y)$ for $i = 1, 2, 3$.

Next we introduce a blurring process by using quaternion operators.

Definition 2. *Suppose* $\mathbf{Q} = Q_0 + Q_1\mathbf{i} + Q_2\mathbf{j} + Q_3\mathbf{k}$ *is a quaternion operator, where* Q_i's *are real blur kernels* ($i = 0, 1, 2, 3$). *A quaternion blur operator on a color image* $\mathbf{u}(x,y)$ *is defined by*

$$
\begin{aligned}
&\mathbf{Q} \circledast \mathbf{u}(x,y)\\
=&-Q_1 \star u_1(x,y) - Q_2 \star u_2(x,y) - Q_3 \star u_3(x,y)\\
&+(Q_0 \star u_1(x,y) - Q_3 \star u_2(x,y) + Q_2 \star u_3(x,y))\mathbf{i}\\
&+(Q_3 \star u_1(x,y) + Q_0 \star u_2(x,y) - Q_1 \star u_3(x,y))\mathbf{j}\\
&-(Q_2 \star u_1(x,y) - Q_1 \star u_2(x,y) - Q_0 \star u_3(x,y))\mathbf{k}.
\end{aligned}
\tag{14}
$$

The blur operator $\mathbf{Q}$ depicts the rendering between color channels. We present a mathematically equivalent characterization of color image blurring, which is feasible to develop fast algorithms. Define

$$
B = \begin{bmatrix} B_{11} & B_{12} & B_{13} & B_{14} \\ B_{21} & & & \\ B_{31} & & \hat{K} & \\ B_{41} & & & \end{bmatrix},
\tag{15}
$$

where B_{ij}'s are arbitrary operators of the same size of K_{ij}'s in (13). Let $Q = (B + J_4BJ_4^T + R_4BR_4^T + S_4BS_4^T)/4$ and $R = (3B - J_4BJ_4^T - R_4BR_4^T - S_4BS_4^T)/4$, where J_4, R_4 and S_4 are unitary operators defined in [20].

Theorem 1. *With the above notation, the cross-channel blurring process* (12) *is equivalent to*

$$
\hat{u}(x,y) = \hat{K} \star u(x,y) = \mathcal{T}(\mathbf{Q} \circledast \mathbf{u}(x,y) + \mathbf{r}(x,y)),
\tag{16}
$$

where quaternion operator $\mathbf{Q} = \Re^{-1}(Q)$ *and quaternion function* $\mathbf{r}(x,y) = \Re_c^{-1}(R \star \Re_c(\mathbf{u}(x,y)))$. *Especially, one quaternion operator satisfying* (16) *is* $\mathbf{Q} = Q_0 + Q_1\mathbf{i} + Q_2\mathbf{j} + Q_3\mathbf{k}$ *with*

$$
\begin{aligned}
Q_0 &= \frac{1}{4}(w_{11}K_{11} + w_{22}K_{22} + w_{33}K_{33}),\\
Q_1 &= \frac{1}{4}(w_{32}K_{32} - w_{23}K_{23}),\\
Q_2 &= \frac{1}{4}(w_{13}K_{13} - w_{31}K_{31}),\\
Q_3 &= \frac{1}{4}(w_{21}K_{21} - w_{12}K_{12}),
\end{aligned}
\tag{17}
$$

where w_{ij} *and* K_{ij} *are given in (13).*

Proof. The proof of Theorem 1 is given in the supplementary material. $\square$

The quaternion blur operator $\mathbf{Q}$ can be interpreted as follows. In the formula (17), the scaling factor $1/4$ is the same in Q_0, Q_1, Q_2 and Q_3. Here Q_0 can be viewed as the sum of the intra-blurring operators K_{ii} according to their corresponding weights w_{ii}, i.e., $w_{11}K_{11} + w_{22}K_{22} + w_{33}K_{33}$. While Q_1, Q_2 and Q_3 can be viewed as the difference of the inter-blurring operators $w_{ij}K_{ij} - w_{ji}K_{ji}$ (or $w_{ji}K_{ji} - w_{ij}K_{ij}$) on the two different color channels ($i \neq j$). It is interesting to note that

when $\hat{K}$ symmetric (i.e., $\hat{K}_{ij} = w_{ij}K_{ij} = w_{ji}K_{ji} = \hat{K}_{ji}$), Q_1, Q_2 and Q_3 are zero matrices. In this case, we refer to color blurring from the i-th channel to the j-th channel is the same as that from the j-th channel to the i-th channel. It is clear that $\mathbf{Q}$ is equal to Q_0, and the resulting output of each channel is equal to $\hat{u}_i = Q_0u_i$ for $i = 1, 2, 3$. Because of color blurring symmetry, we reformulate the whole blurring operator $\hat{K}$ into a simplied real form of $\mathbf{Q}$ such that each channel output is the sum of the intra-blurring operators on each channel input. When $\hat{K}$ is not symmetric, Q_1, Q_2 and Q_3 are not equal to zero and therefore the quaternion blurring operator is not real but the color blurring effect of each imaginary component depends on the difference of the color blurring from the i-th channel to the j-th channel and the color blurring from the j-th channel to the i-th channel.

For comparison, we show the simulations of symmetric motional blur by using $\hat{K}$ and $\mathbf{Q}$ in Figure 1 (b) and (c), respectively. In Figure 1 (d), we show the magnitude difference between the two simulation figures. Similarly, we show the case of asymmetric motional blur in Figure 2.
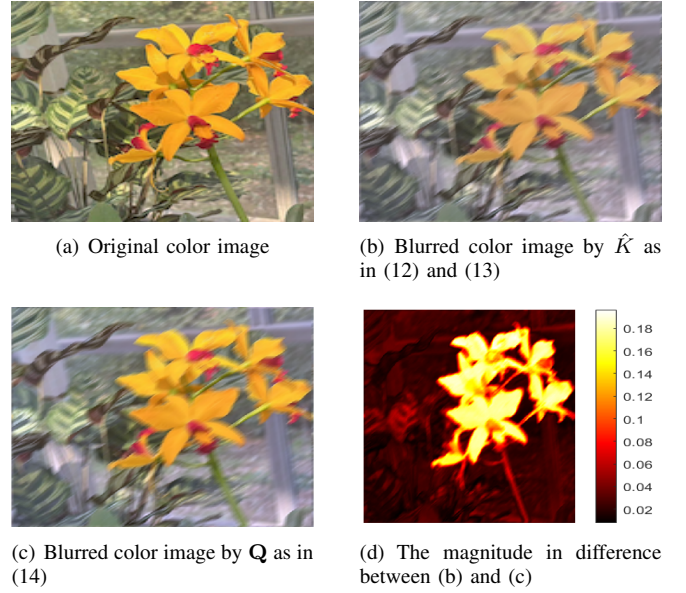

(a) Original color image

(b) Blurred color image by $\hat{K}$ as in (12) and (13)

(c) Blurred color image by $\mathbf{Q}$ as in (14)

(d) The magnitude in difference between (b) and (c)

Fig. 1. A clear picture of the real-world object (Cattleya×hybrida H.J.Veitch) and the simulations of motional blur (length=15, angle=45°, symmetric) by using $\hat{K}$ and $\mathbf{Q}$.

Let us turn back to construct the fidelity term of color image restoration model (11). To reduce different kinds of noise, we define the distance between the observed and original color images by L_p norm as

$$
F(\mathbf{u}, \mathbf{z}, \hat{K}) = \frac{1}{p}\int_\Omega |\hat{K} \star \mathcal{T}(\mathbf{u}) - \mathcal{T}(\mathbf{z})|^p dxdy, \quad p \geq 1.
\tag{18}
$$

According to Theorem 1, we have a quaternion operator form

$$
F(\mathbf{u}, \mathbf{z}, \mathbf{Q}, \mathbf{r}) = \frac{1}{p}\int_\Omega |\mathbf{Q} \circledast \mathbf{u} + \mathbf{r} - \mathbf{z}|^p dxdy, \quad p \geq 1.
\tag{19}
$$

In formula (19), the quaternion convolution operator $\mathbf{Q}$ and the redundant information $\mathbf{r}$ are formed by splitting according to Theorem 1.
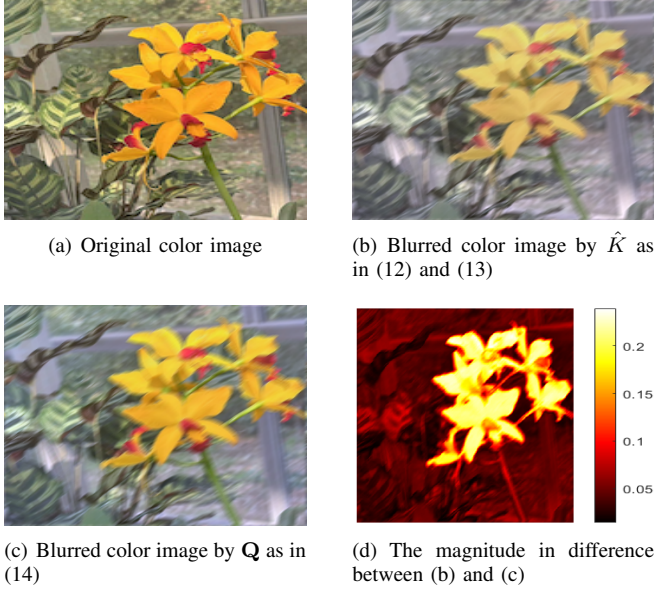
(a) Original color image

(b) Blurred color image by $\hat{K}$ as in (12) and (13)

(c) Blurred color image by $\mathbf{Q}$ as in (14)

(d) The magnitude in difference between (b) and (c)

Fig. 2. A clear picture of the real-world object (Cattleya×hybrida H.J.Veitch) and the simulations of motional blur (length=15, angle=45°, asymmetric) by using $\hat{K}$ and $\mathbf{Q}$.

B. Cross-space total variation regularization functional

The regularization term $J(u,\lambda)$ is a functional of variations in different color spaces of the targeted color image. It aims at extracting cross-channel features of color image, thereby enhancing the preservation of color and texture details. The choice of different regularization functionals is empirical and it relies on the requirement from practical applications. A feasible way to consolidate $J(u,\lambda)$ is to perform a linear combination of all possible regular functionals with parameters and then, to learn the best parameters by machine learning methods. Under the quaternion representation (3), a regularization crossing HSV and RGB color spaces can be defined by

$$J(\mathbf{u},\boldsymbol{\lambda}) = \lambda_1 \text{SVTV}(\mathbf{u}) + \lambda_2 \text{CTV}(\mathcal{T}(\mathbf{u})), \qquad (20)$$

where SVTV is defined by (7), CTV is defined by (8) or (9), and $\lambda_1, \lambda_2 \in \mathbb{R}$. SVTV and CTV correspond to the HSV color space, which is best performant according to the SSIM score, and the RGB color space, which is commonly used in image processing, respectively. Therefore, this CSTV regularization functional can complement each other in terms of color and texture information. There are a number of well-known techniques for dynamically calculating optimal parameters, such as the generalized cross-validation [11], [22], the L-curve method [14] and the discrepancy principle [35]. Here, we generalize the L-curve method to a new L-surface method to determine optimal parameters simultaneously.

The L-surface method is to find a sweet spot on a surface with respect to a certain quality index of the parameter $\boldsymbol{\lambda}$. To be clear, we describe the L-surface method with step size 5×10^{-5} by applying it to determine the optimal $\boldsymbol{\lambda} = (\lambda_1, \lambda_2)$ in (20). Suppose we have an observed color image, say 'statues' in Figure 6, under the setting of Example V-A. The upper bound of parameters is set as $b = 2\sqrt{N\sigma^2} \times 10^{-3}$, where N is

image size and σ is the noise level. The surface of PSNR values of restored color images is plotted in Figure 3 (a) according to $\lambda_1, \lambda_2 \in (0,b)$. High PSNR values are obtained with $\lambda_1 \in (0.4 \times 10^{-3}, b)$ and $\lambda_2 \in (0.2 \times 10^{-3}, 0.5 \times 10^{-3})$ and the highest PSNR value is 27.1903 at $(\lambda_1 = 0.887 \times 10^{-3}, \lambda_2 = 0.222 \times 10^{-3})$. The surface of SSIM values of restored color images is plotted in Figure 3 (b) according to $\lambda_1, \lambda_2 \in (0,b)$. High SSIM values are obtained with $\lambda_1 \in (0.5 \times 10^{-3}, b)$ and $\lambda_2 \in (0.1 \times 10^{-3}, 0.3 \times 10^{-3})$, and the highest SSIM value is 0.7704 at $(\lambda_1 = 0.887 \times 10^{-3}, \lambda_2 = 0.133 \times 10^{-3})$. By the weighted average surface of above PSNR and SSIM surfaces, we obtain the sweet spot $\boldsymbol{\lambda} = (0.887 \times 10^{-3}, 0.222 \times 10^{-3})$ that leads to the optimal combination of SVTV and CTV regularization functionals.
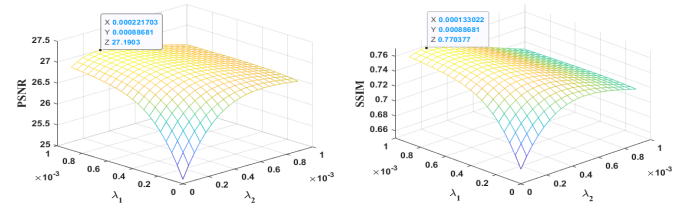
(a) PSNR values in relation to λ_1, λ_2. (b) SSIM values in relation to λ_1, λ_2.

Fig. 3. The values of PSNR and SSIM for the restored image 'statues' in different λ_1, λ_2 conditions.

Obviously, the color image restoration model (11) with $J(\mathbf{u},\boldsymbol{\lambda})$ as in (20) can obtain a broader range of pre-existing knowledge about color image than the model with $\text{SVTV}(\mathbf{u})$ or $\text{CTV}(\mathcal{T}(\mathbf{u}))$. In Figure 3, the PSNR and SSIM values at boundary $\lambda_1 = 0$ or $\lambda_2 = 0$ are smaller than 27.1903 and 0.7704, respectively. So one can conclude that color image restoration models with cross-color space regularization functional perform better than that with single color space regularization functional. With the introduction of cross-color space regularization, more image prior information is available to the former, enriching the ability to interpret color images.

Remark 1. *The SVTV regularization functional defined by* (7) *with* (5) *and* (6) *is based on the quaternion representation of color image in the RGB color space (see [26] and [28]). It reflects the edge and texture information in the HSV color space. So the CSTV regularization functional defined by* (20) *has a quaternion variable in the RGB color space but couples the features in two color spaces.*

C. A new color image restoration model

Now we propose a color image restoration model with a CSTV regularization term and a fidelity with quaternion blur operator. To make a clear description, we concentrate into two color spaces: the widely used RGB color space and the more human eye-perceiving HSV color space.

For an observed image $\mathbf{z}$, a new CSTV regularization model for color image restoration is

$$\hat{\mathbf{u}} = \underset{\mathbf{u}(x,y) \in \mathbb{BV}(\Omega)}{\arg\min} J(\mathbf{u},\boldsymbol{\lambda}) + \frac{1}{p}\int_\Omega |\mathbf{Q}\circledast\mathbf{u} + \mathbf{r} - \mathbf{z}|^p dxdy, \qquad (21)$$

where $J(\mathbf{u}, \boldsymbol{\lambda})$ is defined as in (20) and p is a positive integer not less than 1.

This CSTV regularization model (21) contains one fidelity term and one cross-color space regularization term. The quaternion representation of fidelity term leads to many advantages, such as the values of three color channels of a color pixel are flocked together and their physical meanings are preserved in the whole color image processing based on quaternion computation. On one hand, we utilize quaternion matrices to represent color images. This approach allows for the integrated processing of the red, green, and blue channels of a color image, maintaining the proportional relationships between the channels and effectively preventing the mutual artifacts caused by splitting and recombining the channels. On the other hand, we introduce cross-space total variation regularization. Specifically, we consider the coupling of SVTV and CTV regularization terms, encompassing both the HSV and RGB color spaces. The SVTV and CTV regularization terms effectively preserve edge and texture information within their respective color spaces. The cross-space total variation regularization leverages the strengths of regularization terms from different color spaces, enhancing the breadth and depth of prior information utilized during image restoration.

Especially, color distortion will be hugely reduced in the recovered color image by the new model. The cross-color space regularization functionals complement each other with color and texture information in different color spaces. In this way, the loss of information caused by considering only one color space will be decreased. Parameters λ_1 and λ_2 play in two roles: one is the regularization parameters to balance regularization and fidelity terms, and another is the balance parameters between RGB and HSV color spaces. When $\lambda_1 = 0$, the model degenerates to the classical CTV model; when $\lambda_2 = 0$, the model degenerates to the SVTV model; and when both λ_1 and λ_2 are greater than 0, the information of saturation, value, red, green and blue is used for color image restoration.

Next, we analyze the solvability of the minimization problem (21).

Theorem 2. *There is at least one solution of the CSTV regularization model* (21) *with* $p = 2$ *and moreover, the solution is unique when* $\mathbf{u} \mapsto \mathbf{Q} \circledast \mathbf{u} + \mathbf{r}$ *is injective.*

Proof: If $\mathbf{u}(x, y)$ is a constant value function, then $\mathrm{SVTV}(\mathbf{u}) = 0$ and $\mathrm{CTV}(\mathcal{T}(\mathbf{u})) = 0$. The energy in (21) thus becomes finite. This implies that the infimum of the energy must be finite. Suppose that $\{\mathbf{u}^{(n)}(x, y)\}$ is a minimizing sequence of problem (21). Consequently, a constant $M > 0$ exists such that

$$\mathrm{SVTV}(\mathbf{u}^{(n)}) \leq M.$$

We get that $\left\{ \mathrm{SVTV}(\mathbf{u}^{(n)}) + \sum\limits_{i=1}^{3} \|u_i^{(n)}\|_{L^1} \right\}$ is uniformly bounded by combining the boundedness of $u_1^{(n)}, u_2^{(n)}, u_3^{(n)}$. Noting the compactness referenced in [19], we know that there

exist $u_1^{\min}, u_2^{\min}, u_3^{\min}$ such that

$$u_i^{(n)}(x, y) \xrightarrow{L^1(\Omega)} u_i^{\min}(x, y), \quad u_i^{(n)}(x, y) \to u_i^{\min}(x, y)$$
$$a.e. \ (x, y) \in \Omega, \quad i = 1, 2, 3.$$

Recall that $\mathcal{T}(\mathbf{Q} \circledast \mathbf{u}(x, y) + \mathbf{r}(x, y)) = \hat{K} \star \mathcal{T}(\mathbf{u}(x, y))$. Subsequently, the convergence of the following results is valid:

$$\|\hat{K} \star \mathcal{T}(\mathbf{u}^{(n)}(x, y)) - \mathcal{T}(\mathbf{z}(x, y))\|^2 \to$$
$$\|\hat{K} \star \mathcal{T}(\mathbf{u}^{\min}(x, y)) - \mathcal{T}(\mathbf{z}(x, y))\|^2 \quad a.e. \ (x, y) \in \Omega.$$

Taking advantage of the Fatou's lemma, one has

$$\liminf \int_{\Omega} \|\hat{K} \star \mathcal{T}(\mathbf{u}^{(n)}(x, y)) - \mathcal{T}(\mathbf{z}(x, y))\|^2 dxdy$$
$$\geq \int_{\Omega} \|\hat{K} \star \mathcal{T}(\mathbf{u}^{\min}(x, y)) - \mathcal{T}(\mathbf{z}(x, y))\|^2 dxdy.$$

On account of the lower semi-continuity of $\mathrm{CTV}(\mathcal{T}(\mathbf{u}))$ and $\mathrm{SVTV}(\mathbf{u})$,

$$\liminf \ \mathrm{CTV}(\mathcal{T}(\mathbf{u}^{(n)})) \geq \mathrm{CTV}(\mathcal{T}(\mathbf{u}^{\min})),$$
$$\liminf \ \mathrm{SVTV}(\mathbf{u}^{(n)}) \geq \mathrm{SVTV}(\mathbf{u}^{\min}),$$

then we obtain

$$\liminf \ (\lambda_1 \mathrm{SVTV}(\mathbf{u}^{(n)}) + \lambda_2 \mathrm{CTV}(\mathcal{T}(\mathbf{u}^{(n)}))$$
$$+ \int_{\Omega} \|\hat{K} \star u^{(n)}(x, y) - z(x, y)\|^2 dxdy)$$
$$\geq (\lambda_1 \mathrm{SVTV}(\mathbf{u}^{\min}) + \lambda_2 \mathrm{CTV}(\mathcal{T}(\mathbf{u}^{\min}))$$
$$+ \int_{\Omega} \|\hat{K} \star (\mathcal{T}(\mathbf{u}^{\min}(x, y)) - (\mathcal{T}(\mathbf{z}(x, y))\|^2 dxdy).$$

It leads to the existence of the solution of (21) in the main body. If $\mathbf{u} \mapsto \mathbf{Q} \circledast \mathbf{u} + \mathbf{r}$ ($= \hat{K} \star (\mathcal{T}(\mathbf{u}))$) is injective, the uniqueness of the solution can be obtained quickly by combining the convexity of $\mathrm{SVTV}(\mathbf{u})$ and $\mathrm{CTV}((\mathcal{T}(\mathbf{u}))$. ∎

An important advantage of the CSTV regularization model (21) is that it takes into account the color channels coupling and the local smoothing within each channel. This implicitly leads to achieving better results in terms of both image texture and color fidelity. One can get the explanation from the corresponding Euler-Lagrange (EL) equation. Let $\hat{K}^T$ denote the conjugate transpose of $\hat{K}$ and define $u = \mathcal{T}(\mathbf{u})$. The EL equations of (21) is

$$\frac{\lambda_1}{3} \nabla \cdot \left(\frac{\nabla(Cu)}{\sqrt{(|\partial_x \mathbf{u}|_s^2) + (|\partial_y \mathbf{u}|_s^2)}} + \alpha \frac{\nabla u}{\sqrt{(|\partial_x \mathbf{u}|_v^2) + (|\partial_y \mathbf{u}|_v^2)}} \right)$$
$$+ \lambda_2 \nabla \cdot \frac{\nabla u}{\|\nabla u\|_2} - \left(\hat{K} \star u - \mathcal{T}(\mathbf{z}) \right) \star \hat{K}^T = 0.$$

An interesting finding is that the first two denominators can be further simplified and the gradient of the value component is consistent with that of CTV. The EL equation of (21) becomes

$$\nabla \cdot \left(\lambda_1 \frac{\nabla(Cu)}{\|\nabla(Cu)\|_2} + (\frac{\sqrt{3}}{3} \alpha \lambda_1 + \lambda_2) \frac{\nabla u}{\|\nabla u\|_2} \right) \quad (22)$$
$$- (\hat{K} \star u - \mathcal{T}(\mathbf{z})) \star \hat{K}^T = 0.$$

The EL equation (22) indicates that the proposed model (21) takes into account both the diffusion coefficients of the channel coupling over the saturation and value components and the

diffusion coefficients of the summation of the individual channels over the RGB color space.

To end this section, we present the dual form of model (21)

$$\min_{\mathbf{u}} \max_{\substack{\|g\|\leq 1 \\ \|h\|\leq 1}} \lambda_1 \langle \operatorname{diag}(1,1,\alpha)P\mathcal{T}(\mathbf{u}), \nabla g \rangle + \tag{23}$$

$$\lambda_2 \langle \mathcal{T}(\mathbf{u}), \nabla h \rangle + \tfrac{1}{2}\|\mathbf{Q}\circledast\mathbf{u} + \mathbf{r} - \mathbf{z}\|^2,$$

where

$$P = \begin{bmatrix} \frac{1}{\sqrt{2}} & \frac{-1}{\sqrt{2}} & 0 \\ \frac{1}{\sqrt{6}} & \frac{1}{\sqrt{6}} & \frac{-2}{\sqrt{6}} \\ \frac{1}{\sqrt{3}} & \frac{1}{\sqrt{3}} & \frac{1}{\sqrt{3}} \end{bmatrix}.$$

The solution $\mathbf{u}(x,y)$ of (23) can be differentiable or not, which expands the feasible solution set. The detailed derivation of the EL equation (22) and the dual form (23) is presented in the supplementary material.

IV. FAST AND STABLE ALGORITHM

In this section, we present a new fast and stable algorithm for model (21) based on quaternion operator splitting.

With introducing two auxiliary variables $\mathbf{w}$ and $\mathbf{v}$, we obtain an mathematically equivalent model of (21)

$$\widehat{\mathbf{u}} = \arg\min_{\mathbf{u}} \ \lambda_1 \mathrm{SVTV}(\mathbf{w}) + \lambda_2 \mathrm{CTV}((\mathcal{T}(\mathbf{v}))+$$

$$\tfrac{1}{2}\|\mathbf{Q}\circledast\mathbf{u} + \mathbf{r} - \mathbf{z}\|^2,$$

$$\text{s.t. } \mathbf{w} = \mathbf{u}, \quad \mathbf{v} = \mathbf{u}.$$

The above constrained optimal minimization problem can be converted into an unconstrained problem:

$$\widehat{\mathbf{u}} = \arg\min_{\mathbf{u},\mathbf{w},\mathbf{v}} \ \lambda_1 \mathrm{SVTV}(\mathbf{w}) + \tfrac{\alpha_1}{2}\|\mathbf{w}-\mathbf{u}\|^2+ \tag{24}$$

$$\tfrac{1}{2}\|\mathbf{Q}\circledast\mathbf{u} + \mathbf{r} - \mathbf{z}\|^2 + \lambda_2 \mathrm{CTV}((\mathcal{T}(\mathbf{v})) + \tfrac{\alpha_2}{2}\|\mathbf{v}-\mathbf{u}\|^2,$$

where α_1 and α_2 are two positive parameters. Three unknown variables $\mathbf{u}$, $\mathbf{w}$ and $\mathbf{v}$ can be separated into two independent groups and under the framework of alternating minimization method, problem (24) can be solved by alternatively solving two subproblems:

- **u-subproblem**
  With fixing $\mathbf{w}$ and $\mathbf{v}$, the minimization problem (24) is equivalently reduced to

$$\arg\min_{\mathbf{u}} \ \tfrac{\alpha_1}{2}\|\mathbf{u}-\mathbf{w}\|^2 + \tfrac{\alpha_2}{2}\|\mathbf{u}-\mathbf{v}\|^2+ \tag{25}$$

$$\tfrac{1}{2}\|\mathbf{Q}\circledast\mathbf{u} + \mathbf{r} - \mathbf{z}\|^2.$$

- **(w, v)-subproblem**
  With fixing $\mathbf{u}$, the minimization problem (24) is equivalently reduced to

$$\arg\min_{\mathbf{w},\mathbf{v}} \ \lambda_1 \mathrm{SVTV}(\mathbf{w}) + \tfrac{\alpha_1}{2}\|\mathbf{w}-\mathbf{u}\|^2+ \tag{26}$$

$$\lambda_2 \mathrm{CTV}((\mathcal{T}(\mathbf{v})) + \tfrac{\alpha_2}{2}\|\mathbf{v}-\mathbf{u}\|^2.$$

A. Quaternion operator splitting method for u-subproblem

Now we consider the **u**-subproblem (25) and use its real representation to introduce a quaternion operator splitting method.

From the analysis in Section III-A, the real representation of (25) is

$$\arg\min_{\mathbf{u}} \ \tfrac{\alpha_1}{2}\|\mathbf{u}-\mathbf{w}\|^2 + \tfrac{\alpha_2}{2}\|\mathbf{u}-\mathbf{v}\|^2+ \tag{27}$$

$$\tfrac{1}{2}\|B\Re_c(\mathbf{u}) - \Re_c(\mathbf{z})\|^2,$$

where B is defined by (15). Its normal equation is

$$[B^T B + (\alpha_1+\alpha_2)I]\Re_c(\mathbf{u}) = B^T\Re_c(\mathbf{z}) + \alpha_1\Re_c(\mathbf{w}) + \alpha_2\Re_c(\mathbf{v}). \tag{28}$$

Let $Q = \Re(\mathbf{Q})$ denote the real counterpart of quaternion blur operator $\mathbf{Q}$. The operator B can be splitted into $Q + R$ with setting $R = B - Q$. This implies $B^T B = Q^T Q + Q^T R + R^T R + R^T Q$. An iterative format of (28) is derived as

$$[Q^T Q + (\alpha_1 + \alpha_2)I]\Re_c(\mathbf{u}^{k+1}) = -(Q^T R + R^T Q +$$

$$R^T R)\Re_c(\mathbf{u}^k) + (Q + R)^T\Re_c(\mathbf{z}) + \alpha_1\Re_c(\mathbf{w}) + \alpha_2\Re_c(\mathbf{v}). \tag{29}$$

Let $\mathbf{A} = \Re^{-1}(Q^T Q + (\alpha_1 + \alpha_2)I)$, $\mathbf{x} = \mathbf{u}^{k+1}$ and $\mathbf{b} = \Re_c^{-1}(-(Q^T R + R^T Q + R^T R)\Re_c(\mathbf{u}^k) + (Q + R)^T\Re_c(\mathbf{z}) + \alpha_1\Re_c(\mathbf{w}) + \alpha_2\Re_c(\mathbf{v}))$. Then we can construct an equivalent quaternion linear system of (29),

$$\mathbf{A}\mathbf{x} = \mathbf{b}. \tag{30}$$

So the solution of the **u**-subproblem (25) can be computed by iteratively solving (30). That means we have proposed a quaternion operator splitting method for solving the **u**-subproblem, where the coefficient matrix is splitted into a quaternion operator and a residual operator. This leads to an advantage that the color information of restored color image **u** is preserved by quaternion algebra operations in the solving process.

The core work becomes solving (30). QGMRES [18] is feasible to solve this quaternion linear system. However, we can further apply the Hermitian and positive definite properties of $\mathbf{A}$ to develop a new quaternion conjugate gradient method. Its structure-preserving version is given in Algorithm 1. The quaternion matrix-vector product is implemented by real operation, i.e., $\mathbf{A}\mathbf{x} = \Re_c^{-1}(\Re(\mathbf{A})\Re_c(\mathbf{x}))$.

Algorithm 1 Quaternion Conjugate Gradient Method

1: **Initialization** Set the stopping criteria $tol > 0$ and the initial solution $\mathbf{x}_0 = 0$.
2: $k = 0$, $\mathbf{r}_k = \mathbf{b} - \Re_c^{-1}(\Re(\mathbf{A})\Re_c(\mathbf{x}_k))$ and let $\mathbf{p}_k = \mathbf{r}_k$.
3: **while** $\|\Re_c(\mathbf{r}_k)\|_2 > tol$ **do**
4:     $\mathbf{q}_k = \Re_c^{-1}(\Re(\mathbf{A})\Re_c(\mathbf{p}_k))$,
5:     Compute $a_k = \frac{\langle \mathbf{r}_k, \mathbf{r}_k \rangle}{\langle \mathbf{p}_k, \mathbf{q}_k \rangle}$,
6:     Compute $\mathbf{x}_{k+1} = \mathbf{x}_k + a_k\mathbf{p}_k$,
7:     Compute $\mathbf{r}_{k+1} = \mathbf{r}_k + a_k\mathbf{q}_k$,
8:     Compute $b_k = \frac{\langle \mathbf{r}_{k+1}, \mathbf{r}_{k+1} \rangle}{\langle \mathbf{r}_k, \mathbf{r}_k \rangle}$,
9:     Compute $\mathbf{p}_{k+1} = \mathbf{r}_{k+1} + b_k\mathbf{p}_k$,
10:    $k = k + 1$.
11: **end while**

Remark 2. *Since $Q^T Q$ is symmetric and semi-positive definite, the coefficient matrix $[Q^T Q + (\alpha_1 + \alpha_2)I]$ is surely a symmetric positive definite matrix. These conditions ensure that each inner iteration in solving $\mathbf{x}$ in Algorithm 1 effectively*

reduces the residuals and moves towards a numerical solution. In other words, the convergence and effectiveness of the iterative solution of the $\mathbf{u}$-subproblem are guaranteed.

B. Augmented Lagrangian method for $(\mathbf{w}, \mathbf{v})$-subproblem

Now, we present a new augmented Lagrangian method for solving $(\mathbf{w}, \mathbf{v})$-subproblem (26). Since the two variables are independent of each other and have no intersecting terms, we construct the augmented Lagrangian schemes of computing $\mathbf{w}$ and $\mathbf{v}$, respectively.

- $\mathbf{w}$-subproblem

  With $\mathbf{u}$ and $\mathbf{v}$ fixed, the minimization problem (26) is reduced to

$$\arg\min_{\mathbf{w}} \ \lambda_1 \mathrm{SVTV}(\mathbf{w}) + \frac{\alpha_1}{2}\|\mathbf{w} - \mathbf{u}\|^2. \tag{31}$$

Define $(\mathbf{D}_x\mathbf{w})_{i,j} = \mathbf{w}(i,j) - \mathbf{w}(i-1,j)$, $(\mathbf{D}_y\mathbf{w})_{i,j} = \mathbf{w}(i,j) - \mathbf{w}(i,j-1)$, $\mathbf{s} = P\mathcal{T}(\mathbf{w})$, and $\mathbf{q} = P\mathcal{T}(\mathbf{u})$. By introducing auxiliary variables $t_k^x = D_x s_k$ and $t_k^y = D_y s_k$, we obtain the augmented Lagrangian equation of the $\mathbf{w}$-subproblem (31),

$$
\begin{aligned}
&\frac{\lambda_1}{\alpha_1} \sum_{i=1}^{m}\sum_{j=1}^{n}\left(\sqrt{\sum_{k=1}^{2}|(t_k^x)_{ij}|^2 + |(t_k^y)_{ij}|^2} \right.\\
&\left. + \alpha\sqrt{|(t_3^x)_{ij}|^2 + |(t_3^y)_{ij}^2|}\right) + \frac{1}{2}\|\mathbf{s} - \mathbf{q}\|^2 \\
&+ \sum_{i=1}^{3}[(\tau_i^x, t_i^x - \mathbf{D}_x s_i) + (\tau_i^y, t_i^y - \mathbf{D}_y s_i)] \\
&+ \frac{\beta}{2}\sum_{i=1}^{3}(\|t_i^x - \mathbf{D}_x s_i\|^2 + \|t_i^y - \mathbf{D}_y s_i\|^2),
\end{aligned}
\tag{32}
$$

where τ_i^x and τ_i^y are Lagrangian multipliers and β is a positive penalty parameter.

- $\mathbf{v}$-subproblem

  With $\mathbf{u}$ and $\mathbf{w}$ fixed, the minimization problem (26) is reduced to

$$\arg\min_{\mathbf{v}} \ \lambda_2 \mathrm{CTV}(\mathcal{T}(\mathbf{v})) + \frac{\alpha_2}{2}\|\mathbf{v} - \mathbf{u}\|^2. \tag{33}$$

By introducing auxiliary variables $l_k^x = D_x v_k$ and $l_k^y = D_y v_k$, we obtain the augmented Lagrangian equation of the $\mathbf{v}$-subproblem (33),

$$
\begin{aligned}
&\frac{\lambda_2}{\alpha_2}\sum_{i=1}^{m}\sum_{j=1}^{n}\sqrt{\sum_{k=1}^{3}|(l_k^x)_{ij}|^2 + |(l_k^y)_{ij}|^2} + \frac{1}{2}\|\mathbf{v} - \mathbf{u}\|^2 \\
&+ \sum_{i=1}^{3}((\eta_i^x, l_i^x - \mathbf{D}_x v_i) + (\eta_i^y, l_i^y - \mathbf{D}_y v_i)) \\
&+ \frac{\beta_2}{2}\sum_{i=1}^{3}(\|l_i^x - \mathbf{D}_x v_i\|^2 + \|l_i^y - \mathbf{D}_y v_i\|^2).
\end{aligned}
\tag{34}
$$

where η_i^x and η_i^y are Lagrangian multipliers and β_2 is a positive penalty parameter.

The solutions of (31) and (33) can be computed by many well-known methods; see [2], [19] for instance. Overall, the $(\mathbf{w}, \mathbf{v})$-subproblem needs to compute several soft shrinkage

functions and solve two real linear systems. According to the classic framework of the ADMM [7], [8], we construct a method to solve (32) and (34) within three steps in the supplementary material.

C. A new fast and stable algorithm based on quaternion operator splitting

Now we present a new algorithm for model (21) based on the methods in Sections IV-A and IV-B. The puedo code is given in Algorithm 2.

Algorithm 2 Quaternion Operator Splitting Method

1: **Initialization** Choose parameters $\lambda_1, \lambda_2, \alpha_1, \alpha_2, \ \tau_i^x, \tau_i^y$ and $\eta_i^x, \eta_i^y \ (i = 1, 2, 3), \alpha, \beta$. Set the stopping criteria $tol > 0$ and $\mathbf{u}^0 = \mathbf{0}, \ \mathbf{w}^0 = \mathbf{z}, \mathbf{v}^0 = \mathbf{z}, err = 1, err_u = 1, l = 0$.
2: **while** $err > tol$ **do**
3:    $k = 0, \mathbf{u}^k = \mathbf{u}^l$
4:    **while** $err_u > tol$ **do**
5:       Solve $\mathbf{u}^{k+1}$ by (30) using Algorithm 1,
6:       $k = k + 1$,
7:       Compute $err_u = \frac{\|\mathbf{u}^{k-1} - \mathbf{u}^k\|_2^2}{\|\mathbf{u}^{k-1}\|_2^2}$,
8:    **end while**
9:    $\mathbf{u}^{l+1} = \mathbf{u}^k$,
10:   Update $\mathbf{w}^{l+1}$ by solving (31),
11:   Update $\mathbf{v}^{l+1}$ by solving (33),
12:   $l = l + 1$,
13:   Compute $err = \frac{\|\mathbf{v}^{l-1} - \mathbf{v}^l\|_2^2}{\|\mathbf{v}^{l-1}\|_2^2}$.
14: **end while**

The main idea of Algorithm 2 is to alternately solve (25) and (26) with proper initial values. The only problem left for discussion is how to determine their augmented Lagrange parameters α_i's. This is one of the well-known parameter-selection problems that stand for a long history. Here, we apply the newly proposed L-surface method in Section III-B to determine the optimal α_i's. These parameters are determined using a few typical images before running before running Algorithm 2 and, once determined, are used to process all images of the same degradation type.

Now we demonstrate the parameter selection process of α_i's by the L-surface method with step size 2×10^{-2} in Section III-B. Suppose that we have obtained an observed color image, say 'statues' in Figure 6, under the setting of Example V-A. In case of taking CIEde2000 value as a criterion, we plot the surface of CIEde2000 values according to $\alpha_1, \alpha_2 \in [0, 0.4]$ of restored color images in Figure 4. The optimal parameter is $\alpha_1 = 0.28$, $\alpha_2 = 0.06$ at which the minimum CIEde2000 value reaches 3.1410.

We have proposed a fast and stable algorithm (Algorithm 2) to solve the CSTV regularization model for cross-channel deblurring problem. This idea of quaternion characterization of blurring and quaternion operator splitting can also be applied to improve the well-known color image restoration models such as CTV and SVTV. The numerical comparison will be given in Section V-C.
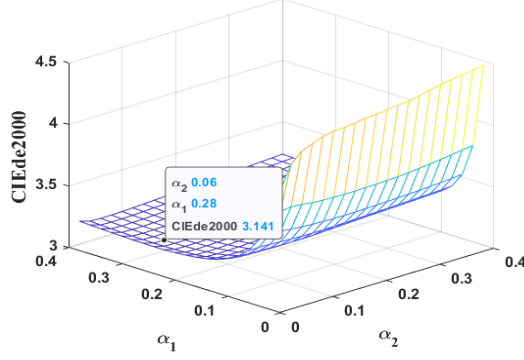
Fig. 4. The values of CIEde2000 for the restored image 'statues' in different α_1 and α_2 conditions.

V. NUMERICAL EXPERIMENTS

In this section, we consider various types of cross-channel blur kernels and weight matrices to illustrate the validity of the proposed model and algorithms. We compare the proposed CSTV regularization model and Algorithm 2 (referred to as CSTV) with CTV_1 [1], CTV_2 [2], SVTV [19], the split-algorithm-based CTV ($\text{CTV}_{\text{split}}$) [36], MTV [37], by applying them to solve cross-channel deblurring problems. As in [19], we choose the optimal values of the regularization parameters in terms of PSNR for all the compared methods. All experiments were implemented by MATLAB (R2020a) on a computer with Intel(R) Xeon(R) CPU E5-2630 @ 2.40Ghz/32.00 GB. The stopping criterion for all these iterative methods is that the norm of the successive iterations is less than 1.0×10^{-5}.

We use the ground truth images of size $n \times n$ shown in Figure 5 with $n = 512$. Let $\mathbf{U}$ and $\hat{\mathbf{U}}$ denote the original and restored color images, respectively. The quality of the restored color image is indicated by the four standard criteria: PSNR, SSIM, MSE, and CIEde2000. PSNR means the peak signal-to-noise ratio value of $\hat{\mathbf{U}}$, defined by

$$\text{PSNR}(\hat{\mathbf{U}}, \mathbf{U}) = 10 * \log_{10}\left(\frac{255^2 n^2}{\|\hat{\mathbf{U}} - \mathbf{U}\|_F^2}\right).$$

SSIM denotes the structural similarity index [34] of $\hat{\mathbf{U}}$ and $\mathbf{U}$, defined by

$$\text{SSIM}(\hat{\mathbf{U}}, \mathbf{U}) = \frac{(4\mu_x\mu_y + c_1)(2\sigma_{xy} + c_2)}{(\mu_x^2 + \mu_y^2 + c_1)(\sigma_x^2 + \sigma_y^2 + c_2)},$$

where x and y respectively stand for the vector forms of $\hat{\mathbf{U}}$ and $\mathbf{U}$, $c_{1,2}$ are two constants, $\mu_{x,y}$ signify the averages of x and y, and $\sigma_{x,y}^2$ stand for the variances of x and y, and σ_{xy} denotes the covariance between x and y. MSE is the mean square error value of $\hat{\mathbf{U}}$, defined by

$$\text{MSE}(\mathbf{U}_m, \mathbf{U}) = \frac{\|\hat{\mathbf{U}} - \mathbf{U}\|_F^2}{n^2}.$$

The CIEde2000 color difference formula is described in [30], which is used to evaluate the color difference between the original and the restored image.
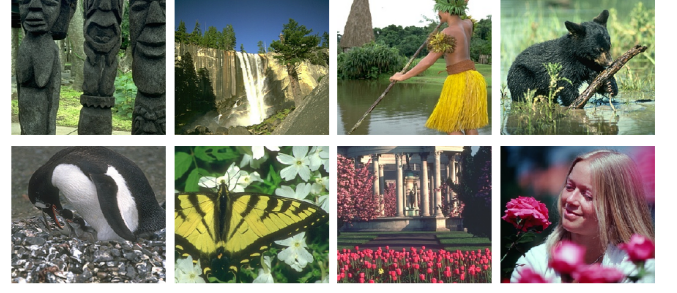
Fig. 5. Ground truth images.

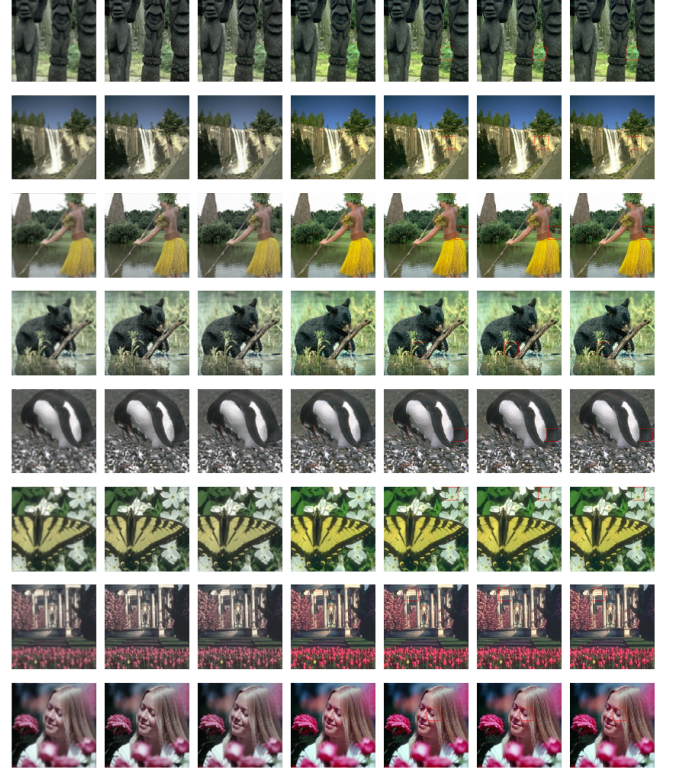Fig. 6. Visual comparison of six methods in symmetric cross-channel deblurring. From left to right: Observed images and restorations by CTV_1, CTV_2, $\text{CTV}_{\text{split}}$, MTV, SVTV and CSTV. (Color images have been reduced to save space. The same applies hereinafter.)
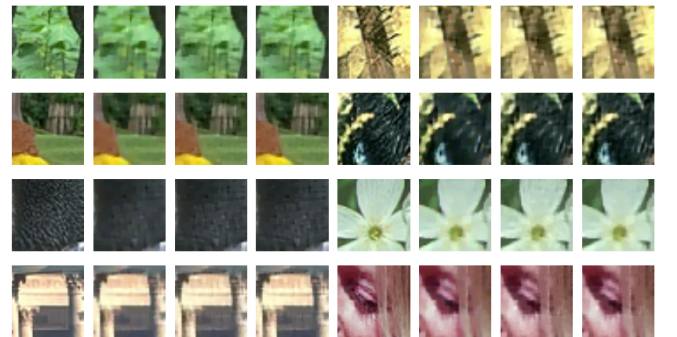

Fig. 7. Corresponding zooming parts of original image and restorations by MTV, SVTV and CSTV given in Figure 6.

TABLE I
PSNR, SSIM, MSE AND CIEDE2000 VALUES OF THE RESTORED COLOR IMAGES IN SECTION V-A.

Observed image (PSNR SSIM)	Method	PSNR	SSIM	MSE (1×10^{-3})	CIEde2000	Observed image (PSNR SSIM)	Method	PSNR	SSIM	MSE (1×10^{-3})	CIEde2000
statues (22.6920 0.5002)	CTV_1	24.7890	0.6817	3.3197	6.3750	waterfall (21.3554 0.5654)	CTV_1	22.9317	0.7027	5.0914	7.5840
	CTV_2	24.7416	0.6740	3.3561	6.1065		CTV_2	22.8933	0.7097	5.1365	7.4116
	CTV_{split}	26.1593	0.6983	2.4214	3.9703		CTV_{split}	25.2652	0.7541	2.9749	3.7826
	MTV	26.9277	0.7374	2.0288	4.0883		MTV	26.3011	0.8008	2.3426	3.7302
	SVTV	27.3926	0.7688	1.8228	3.1326		SVTV	26.6554	0.8156	2.1601	3.2863
	CSTV	27.4356	0.7718	1.8048	3.1611		CSTV	26.7418	0.8169	2.1175	3.1879
aborigine (21.1179 0.5610)	CTV_1	22.3146	0.7152	5.8687	7.2164	bear (20.2929 0.5507)	CTV_1	21.9875	0.7154	6.3278	8.1320
	CTV_2	22.29382	0.7181	5.8968	7.0597		CTV_2	21.9315	0.7134	6.4098	8.0203
	CTV_{split}	26.8057	0.7673	2.0866	3.3089		CTV_{split}	23.3130	0.7477	4.6634	4.3142
	MTV	27.7981	0.8107	1.6603	3.3228		MTV	24.3554	0.7907	3.6683	4.3680
	SVTV	28.1841	0.8285	1.5191	2.7941		SVTV	24.7129	0.8108	3.3784	3.8824
	CSTV	28.2283	0.8293	1.5037	2.7419		CSTV	24.8641	0.8111	3.2628	3.7156
penguin (21.8428 0.6083)	CTV_1	24.1892	0.7349	3.8113	5.7218	butterfly (20.9821 0.6702)	CTV_1	22.6934	0.7702	5.3785	7.8815
	CTV_2	24.1561	0.7389	3.8405	5.3536		CTV_2	22.6994	0.7789	5.3710	7.7457
	CTV_{split}	25.3151	0.7760	2.9410	4.5552		CTV_{split}	26.8852	0.8355	2.0487	3.0992
	MTV	26.5423	0.8079	2.2170	4.7076		MTV	28.3685	0.8672	1.4560	3.0369
	SVTV	26.8982	0.8206	2.0426	3.4735		SVTV	28.3065	0.8637	1.4769	2.8690
	CSTV	26.9406	0.8209	2.0228	3.5037		CSTV	28.4958	0.8734	1.4139	2.5785
garden (19.4933 0.5176)	CTV_1	21.6959	0.7188	6.7673	7.7463	girl (22.5950 0.6946)	CTV_1	24.0889	0.7844	3.9004	6.9659
	CTV_2	21.6205	0.7167	6.8857	7.5397		CTV_2	24.0870	0.7941	3.9021	6.7890
	CTV_{split}	23.7840	0.7741	4.1841	4.9869		CTV_{split}	28.5861	0.8430	1.3848	2.8742
	MTV	25.2706	0.8354	2.9712	4.9658		MTV	29.5834	0.8634	1.1007	2.9632
	SVTV	25.4766	0.8478	2.8336	4.6447		SVTV	29.7902	0.8687	1.0495	2.5738
	CSTV	25.6999	0.8494	2.6916	4.1641		CSTV	29.8912	0.8735	1.0254	2.4027

A. Symmetric cross-channel deblurring problem

In this example, we consider the case where all sub-blur kernels are identical and the weight matrix is symmetric. The degraded images used for testing are generated by applying the cross-channel blur $\hat{K} = K \odot W$ with Gaussian blur $K = ones(3,3) \otimes (G,5,5)$ and weight matrix

$$W = \begin{bmatrix} 0.7 & 0.15 & 0.15 \\ 0.15 & 0.7 & 0.15 \\ 0.15 & 0.15 & 0.7 \end{bmatrix}$$

and Gaussian noise with standard deviation $\sigma = 0.01$ to the clean color images. The observed images after degradation process are listed in the first column of Figure 6.

We apply six compared method to the blurred and noised color images and use the newly proposed L-surface method to choose optimal model parameters. The evaluation criteria values of the restored color images are listed in Table I with the best values in bold and the secondly best ones underlined. One can see that the newly proposed CSTV achieves at the best PSNR, SSIM and MSE values among six methods. SVTV performs slightly worse than CSTV, and in particular, it outperforms CSTV on the CIEde2000 values of two testing color images 'statues' and 'penguin'.

The restorations of six methods are given in Figure 6. These numerical results indicate that all of them successfully solved the symmetric cross-channel deblurring problem and recovered color images at a high level. When looking at details of colors and textures, one can see that CSTV performs better than other five methods. The color images restored by CTV_1 and CTV_2 have distorted colors. The restorations of CTV_{split} still have some artifacts; for instance, see the grass skirt detail in 'aborigine' and the watercress in 'bear'. MTV has achieved relatively good results both visually and numerically. However, MTV seems oversmoothing in some small details; see the flower texture in the upper right corner of the 'butterfly'. Under the same stopping criterion, CSTV restores color images with faithful colors and textures and without artifacts and color artifacts. The best performance of CSTV numerically verifies its advantages in treating color pixel as a quaternion number and using quaternion operator splitting method.

To further highlight the differences of CSTV to MTV and SVTV, we enlarge the local features of their restorations in Figure 7. The corresponding zoomed parts are indicated by red boxes in Figure 6. The amplification of local features reveals that CSTV retains more texture detail; see the tip of a tree branch in 'waterfall', the texture of petals in 'butterfly', and the details of the letters in 'garden'. Additionally, we can see color artifacts at the edges of color images restored by MTV, including the hair part in 'girl', the left edge of the flower in 'butterfly', and the lower half of the fence in 'aborigine'.

B. Asymmetric cross-channel deblurring problem

In this example, we consider the restorations of six compared methods when the sub-blur kernels are different and the weight matrix is asymmetric. The degraded images are generated by introducing the cross-channel blur $\hat{K} = K \odot W$ with

$$K = \begin{bmatrix} (A,5) & (M,11,45) & (M,21,90) \\ (M,11,45), & (A,5) & (G,5,5) \\ (M,21,90) & (G,5,5) & (A,5) \end{bmatrix}$$

and

$$W = \begin{bmatrix} 0.7 & 0.15 & 0.15 \\ 0.1 & 0.8 & 0.1 \\ 0.05 & 0.05 & 0.9 \end{bmatrix}$$

and Gaussian noise with standard deviation $\sigma = 0.01$ to original color images. This blur operator is a mixture of Gaussian blur $(G,5,5)$, motion blur $(M,11,45)$ and average blur $(A,5)$.

In Figure 8, we display the observed color images and the restored color images by the six methods. These numerical results indicate that the asymmetric cross-channel deblurring problem is difficult for CTV_1, CTV_2 and CTV_{split}. Visually, the restorations of CTV_1 and CTV_2 still contain

TABLE II
PSNR, SSIM, MSE AND CIEDE2000 VALUES OF THE RESTORED COLOR IMAGE IN SECTION V-B.

| Observed image (PSNR SSIM)	Method	PSNR	SSIM	MSE (1×10^{-3})	CIEde2000	Observed image (PSNR SSIM)	Method	PSNR	SSIM	MSE (1×10^{-3})	CIEde2000
statues (22.8211 0.4890)	CTV_1	24.8674	0.6587	3.2603	5.7584	waterfall (21.87546 0.5683)	CTV_1	23.5651	0.6927	4.4004	6.0229
	CTV_2	24.8129	0.6510	3.3015	5.4356		CTV_2	23.5176	0.7005	4.4488	5.8441
	CTV_{split}	18.6735	0.6336	13.572	14.4771		CTV_{split}	16.2687	0.6819	23.612	15.3867
	MTV	26.7807	0.7275	2.0986	4.3106		MTV	26.3129	0.7962	2.3373	3.8289
	SVTV	27.4255	0.7674	1.8091	3.0850		SVTV	26.9149	0.8197	2.0347	3.1820
	CSTV	27.4570	0.7703	1.7960	3.1961		CSTV	27.0396	0.8152	1.9772	3.1800
aborigine (22.3385 0.5643)	CTV_1	23.8554	0.7054	4.1159	6.0587	bear (20.4969 0.5420)	CTV_1	22.1822	0.6965	6.0504	6.6658
	CTV_2	23.8243	0.7091	4.1454	5.8796		CTV_2	22.1152	0.6947	6.1443	6.5229
	CTV_{split}	15.1137	0.6704	30.805	15.6282		CTV_{split}	14.9329	0.6858	32.115	18.1410
	MTV	27.7450	0.8013	1.6808	3.4535		MTV	24.5403	0.7876	3.5153	4.5132
	SVTV	28.3032	0.8261	1.4780	2.7616		SVTV	25.1865	0.8173	3.0293	3.7226
	CSTV	28.4469	0.8268	1.4300	2.7396		CSTV	25.3409	0.8188	2.9234	3.5917
penguin (21.5152 0.5904)	CTV_1	23.6758	0.7131	4.2896	6.1883	butterfly (21.5967 0.6596)	CTV_1	23.6836	0.7609	4.2819	6.1226
	CTV_2	23.6289	0.7171	4.3362	5.7965		CTV_2	23.6712	0.7694	4.2942	5.9530
	CTV_{split}	16.1198	0.7181	24.435	20.1197		CTV_{split}	15.4844	0.7548	2.8285	14.9422
	MTV	26.3597	0.7989	2.3122	4.9455		MTV	28.2452	0.8625	1.4979	3.1680
	SVTV	26.8866	0.8171	2.0480	3.4193		SVTV	28.4956	0.8673	1.4140	2.7874
	CSTV	26.9257	0.8172	2.0297	3.5165		CSTV	28.5637	0.8730	1.3920	2.5219
garden (19.4949 0.5044)	CTV_1	21.5268	0.6970	7.0359	7.5611	girl (23.0120 0.6945)	CTV_1	24.6124	0.7778	3.4503	6.2335
	CTV_2	21.4425	0.6941	7.1738	7.3168		CTV_2	24.6185	0.7885	3.4526	6.0251
	CTV_{split}	16.6254	0.6942	21.750	18.7589		CTV_{split}	16.4629	0.7647	22.579	18.9103
	MTV	25.0593	0.8270	3.1194	5.2695		MTV	29.3705	0.8552	1.1560	3.1128
	SVTV	25.7302	0.8510	2.6729	4.4351		SVTV	29.8001	0.8665	1.0471	2.5057
	CSTV	25.9486	0.8459	2.5418	4.1440		CSTV	29.8680	0.8695	1.0309	2.4164
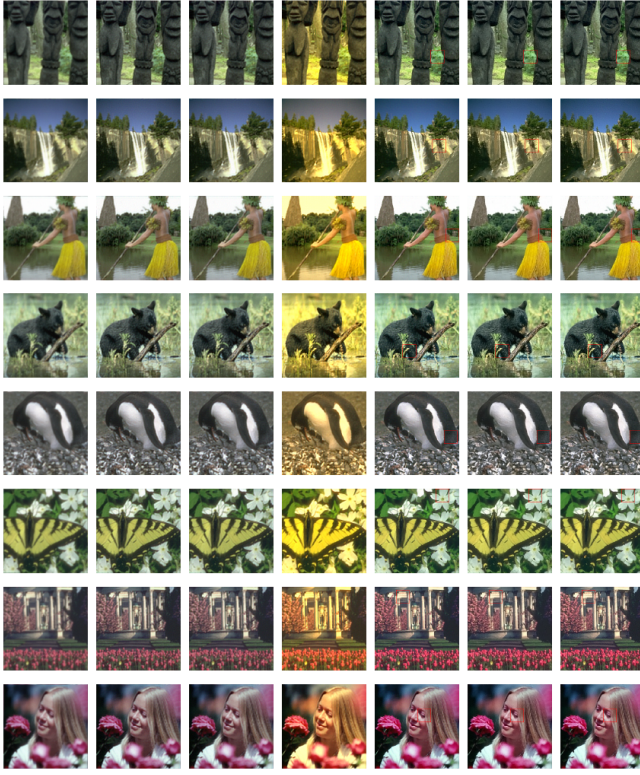
Fig. 8. Visual comparison of six methods in asymmetric cross-channel deblurring. From left to right: Observed images and restorations by CTV_1, CTV_2, CTV_{split}, MTV, SVTV, CSTV.

Fig. 9. Corresponding zooming parts of the original color images and the restorations of MTV, SVTV and CSTV given in Figure 8.

cross-channel blurred color pixels and a slight color shift. For example, the texture of the grass skirt in 'aborigine' is relatively smooth and darker overall. The color images restored by CTV_{split} have a significant color shift in this design of asymmetric weight matrix and different sub-blur kernels. Fortunately, the other three methods MTV, SVTV and CSTV are able to solve such asymmetric cross-channel deblurring
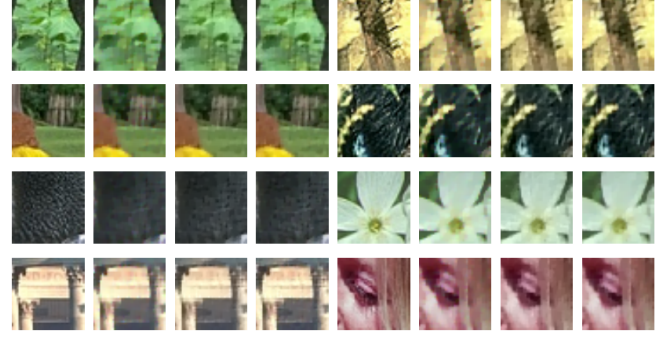
problem. We zoom in the local details of the restorations of them (the zoomed areas are indicated by red boxes in Figure 8) in Figure 9. Visually, the proposed CSTV achieves the best restorations that preserve the geometric textures and color information. From the comparison of the skin detail in 'aborigine' and the petal textures in 'butterfly', we can see that CSTV produces better texture features, while the MTV tend to oversmooth. Also, CSTV produces superior results in terms of color fidelity judging from the branch edges in 'waterfall' and the petal edges in 'butterfly', where the MTV tends to have color artifacts in the sharply changing areas of the images.

We present the PSNR, SSIM, MSE, and CIEde2000 values of the color images restored by six compared methods in Table II with the best values in bold and the secondly best ones underlined. One can evidently observe that the new approach CSTV achieves the best average values of PSNR, SSIM, MSE and CIEde2000. Especially, CSTV has an average minimum reduction of CIEde2000 around 0.64 compared with the other five methods. From the comparison between Tables I and II, it is worth emphasizing that the restoration numerical results

of MTV are worse than the corresponding results in Example V-A in terms of indicators such as CIEde2000, while those of CSTV are more stable for the restorations of different blur kernels. This means that MTV is more sensitive to the design of cross-channel blur kernel and CSTV is more general and stable. These numerical results support the efficiency, stableness and superiority of the newly proposed CSTV.

In addition, we compare the performance of above methods at different levels of noise. We take 'butterfly' as the testing color image and set the noise levels as 0.05, 0.1 and 0.5. The numerical results are given in Table III. Note that the notation '-' means that CTV_1, CTV_2 and MTV fail to compute acceptable restorations in the third case. One can see that the newly proposed CSTV performs better than the other compared methods at color image deblurring with different levels of noise. The restored color images and parameter values are presented in the supplementary material.

TABLE III
NUMERICAL VALUES FOR THE CASES WITH DIFFERENT LEVELS OF NOISE IN SECTION V-B.

Noise level	Method	PSNR	SSIM	MSE (1×10^{-3})	CIEde2000
0.05	CTV_1	20.8483	0.4866	8.2260	12.3094
	CTV_2	21.1753	0.5092	7.6290	11.6168
	MTV	24.7291	0.7493	3.3660	4.9102
	SVTV	<u>24.8010</u>	<u>0.7627</u>	<u>3.3110</u>	<u>4.2139</u>
	CSTV	**24.9349**	**0.7631**	**3.2100**	**4.1395**
0.1	CTV_1	16.9792	0.2985	20.0480	19.3420
	CTV_2	17.3635	0.3126	18.3500	18.6192
	MTV	20.5315	0.4967	8.8480	11.2231
	SVTV	<u>23.2933</u>	<u>0.6974</u>	<u>4.4850</u>	**5.2823**
	CSTV	**23.4325**	**0.7009**	**4.5370**	<u>5.3292</u>
0.5	CTV_1	-	-	-	-
	CTV_2	-	-	-	-
	MTV	-	-	-	-
	SVTV	<u>18.3643</u>	<u>0.4124</u>	<u>14.5740</u>	<u>13.4633</u>
	CSTV	**18.5622**	**0.4221**	**13.9240**	**13.3424**

C. Analysis of cross-channel deblurring ability

In this example, we elucidate the benefits of using quaternion characterization of blurring and quaternion operator splitting method. The observed image ('butterfly') is solely affected by a blurring operator, without any distortion caused by noise. The chosen blur operators are Gaussian blur $ones(3,3) \otimes (G,5,5)$, motion blur $ones(3,3) \otimes (M,11,45)$ and average blur $ones(3,3) \otimes (A,5)$ with weight matrix

$$W = \begin{bmatrix} 0.7 & 0.15 & 0.15 \\ 0.15 & 0.7 & 0.15 \\ 0.15 & 0.15 & 0.7 \end{bmatrix}.$$

Our discussion encompasses two facets: regularization and algorithm. We denote the CSTV regularization model (21) with quaternion operator splitting solver (Algorithm 2) by $CSTV_{QGMRES}$. From the regularization aspect, we test two special cases of the CSTV regularization model (21): $SVTV_{QGMRES}$ $(\lambda_1 > 0, \lambda_2 = 0)$ and CTV_{QGMRES} $(\lambda_1 = 0, \lambda_2 > 0)$. For the algorithm aspect, we change the fidelity term (19) to the fidelity term (18) and solve model (21) by the real ADMM method with GMRES solver. This version uses only real operator algorithms and does not use quaternion operator algorithms. We denote it by $CSTV_{GMRES}$ and denote

its two special cases by $SVTV_{GMRES}$ $(\lambda_1 > 0, \lambda_2 = 0)$ and CTV_{GMRES} $(\lambda_1 = 0, \lambda_2 > 0)$.

The numerical results in the aforementioned six cases are presented in Table IV. One can easily find that the performance of the proposed CSTV regularization model is significantly higher than the corresponding results of the single (SVTV or CTV) regularization model in each evaluation index. For CTV_{GMRES}, $SVTV_{GMRES}$ and $CSTV_{GMRES}$, the PSNR value can be increased by approximately 1.4, the SSIM value can be improved by up to 7.27%, the MSE value can be reduced by as much as 31.5%, and the CIEde2000 value can be decreased by up to 16.9%. For CTV_{QGMRES}, $SVTV_{QGMRES}$ and $CSTV_{QGMRES}$, the PSNR value can be increased by an average of approximately 1, the SSIM value can be improved by up to 3.57%, the MSE value can be reduced by as much as 27.5%, and the CIEde2000 value can be decreased by up to 10.9%.

When examining the algorithm for model resolution, it becomes visually evident from Table IV that the quaternion operation process (CTV_{QGMRES}, $SVTV_{QGMRES}$ and $CSTV_{QGMRES}$) significantly enhances the corresponding evaluation metrics of color images deblurred by the real operation process (CTV_{GMRES}, $SVTV_{GMRES}$ and $CSTV_{GMRES}$). Averagely, the PSNR value sees an increase of 2.4, the SSIM value improves by 0.06, the MSE value decreases by 1.5e-4, and the CIEde2000 value reduces by 0.72.

The deblurred color images in the aforementioned six cases are presented in Figure 10 and the zoomed parts are shown in Figure 11. One can find that color images deblurred by $CSTV_{QGMRES}$ can better restore the details, such as maintaining the continuity of the lines. Moreover, the feature details restored by $CSTV_{QGMRES}$ under quaternion operations become even more striking than those by $CSTV_{GMRES}$ under real operations.

In order to further illustrate the advantages of algorithms, we show the step-by-step results $\mathbf{u}_k$ of the restoration process using $CSTV_{GMRES}$ and $CSTV_{QGMRES}$ in Figures 12 and 13. In Figure 14, we show the comparison results of PSNR, SSIM, MSE and CIEde2000 values corresponding to the step-by-step result $\mathbf{u}_k$ during the restoration process. $CSTV_{QGMRES}$ converges in 41 iteration steps and $CSTV_{GMRES}$ convergences in 24 iteration steps. The average CPU time for a single-step iteration of $CSTV_{QGMRES}$ is 2.7931 seconds and that of $CSTV_{GMRES}$ is 1.4757 seconds. However, the restoration of $CSTV_{QGMRES}$ achieve higher quality than that of $CSTV_{GMRES}$. At the starting, the PSNR, SSIM, MSE and CIEde2000 values of the former are not better than those of the latter. After a few of iterations, $CSTV_{QGMRES}$ performs much better than $CSTV_{GMRES}$.

For the above analysis, we can make two key assertions:
- Firstly, the deblurring efficiency of the CSTV regularization model is markedly superior to that of the CTV or SVTV regularization model under identical parameter settings.
- Secondly, the CTV, SVTV and CSTV regularization models with applying quaternion blur operation $\mathbf{Q}$ significantly outperform their counterparts with applying real blur operation $\hat{K}$ under the same parameter settings.

TABLE IV
PSNR, SSIM, MSE AND CIEde2000 VALUES OF THE DEBLURRED COLOR IMAGES IN SECTION V-C.

Blur type	Method	PSNR	SSIM	MSE (1×10^{-3})	CIEde2000
Gaussian	$\text{CTV}_{\text{GMRES}}$	27.5742	0.8566	1.7482	2.4202
	$\text{SVTV}_{\text{GMRES}}$	27.9638	0.8598	1.5981	2.3634
	$\text{CSTV}_{\text{GMRES}}$	**28.9120**	**0.8878**	**1.2847**	**2.0897**
Gaussian	$\text{CTV}_{\text{QGMRES}}$	30.1270	0.9109	0.97119	1.8073
	$\text{SVTV}_{\text{QGMRES}}$	30.2314	0.9040	0.94812	1.8845
	$\text{CSTV}_{\text{QGMRES}}$	**30.9028**	**0.9230**	**0.81231**	**1.7156**
Motion	$\text{CTV}_{\text{GMRES}}$	25.8199	0.8111	2.6183	3.2780
	$\text{SVTV}_{\text{GMRES}}$	26.4653	0.8263	2.2567	3.0875
	$\text{CSTV}_{\text{GMRES}}$	**27.5577**	**0.8570**	**1.7948**	**2.7253**
Motion	$\text{CTV}_{\text{QGMRES}}$	29.0774	0.8897	1.2367	2.2995
	$\text{SVTV}_{\text{QGMRES}}$	29.6386	0.8914	1.0868	2.2388
	$\text{CSTV}_{\text{QGMRES}}$	**30.4742**	**0.9129**	**0.89655**	**2.0485**
Average	$\text{CTV}_{\text{GMRES}}$	23.5221	0.6974	4.4442	4.2445
	$\text{SVTV}_{\text{GMRES}}$	23.9698	0.7142	4.0088	4.0452
	$\text{CSTV}_{\text{GMRES}}$	**24.6607**	**0.7481**	**3.4193**	**3.6768**
Average	$\text{CTV}_{\text{QGMRES}}$	25.5468	0.7853	2.7882	3.2664
	$\text{SVTV}_{\text{QGMRES}}$	25.8810	0.7869	2.5816	3.2145
	$\text{CSTV}_{\text{QGMRES}}$	**26.2855**	**0.8124**	**2.3521**	**3.0027**

Fig. 10. From left to right: the observed color images and the deblurred color images by $\text{CTV}_{\text{GMRES}}$, $\text{SVTV}_{\text{GMRES}}$, $\text{CSTV}_{\text{GMRES}}$, $\text{CTV}_{\text{QGMRES}}$, $\text{SVTV}_{\text{QGMRES}}$ and $\text{CSTV}_{\text{QGMRES}}$. The first row is for Gaussian blur, the second row is for motion blur, and the third row is average blur.

VI. CONCLUSION

In this paper, we have proposed a novel CSTV regularization model for cross-channel deblurring problem of color images. The proposed model contains a new joint regularization term that exploits the complementary information of two or more different color spaces such as RGB and HSV. It also has a new fidelity term that is characterized by quaternion blur operators. A new fast and stable quaternion operator splitting algorithm is proposed to solve the proposed CSTV regularization model. The advantages of the newly defined regularization and fidelity terms are explained in theory and are verified in numerical examples.

The proposed model and algorithm form a general framework that provides new ideas to improve many color TV-based models for color image restoration. We believe that there is still room for further optimization of our model by introducing the variational contrast enhancement method in [27]. In future, we will consider this valuable topic and apply our method to study the blind cross-channel deblurring problem.

ACKNOWLEDGMENT

Fig. 11. Zoomed parts of color images in Figure 10.

Fig. 12. Restorations at iteration step k (k=1, 4, 7, 10, 13, 16, 19, 22, 24) of the deblurring process by $\text{CSTV}_{\text{GMRES}}$.

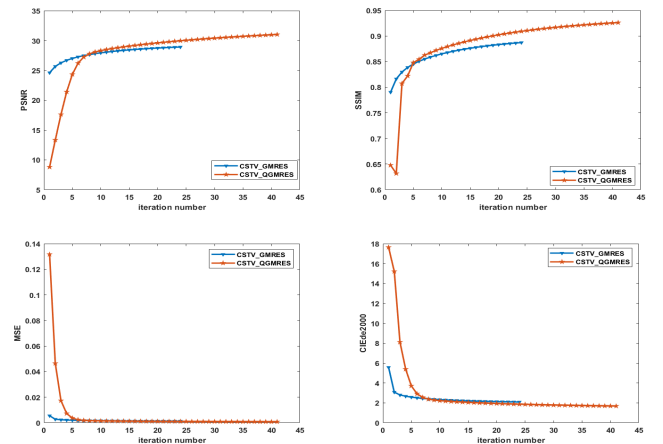Fig. 13. Restorations at iteration step k (k=1, 4, 7, 10, 13, 16, 19, 22, 25, 28, 31, 34, 37, 41) of the deblurring process by $\text{CSTV}_{\text{QGMRES}}$.

Fig. 14. PSNR, SSIM, MSE and CIEde2000 values of color images computed by $\text{CSTV}_{\text{GMRES}}$ and $\text{CSTV}_{\text{QGMRES}}$ at iteration step k.

REFERENCES

[1] T. Blomgren and T. Chan. Color TV: Total variation methods for restoration of vector valued images, *IEEE Trans. Image Process.*, 7: 304–309, 1998.

[2] X. Bresson and T. Chan. Fast dual minimization of the vectorial total variation norm and applications to color image processing, *Inverse Probl. Imag.*, 2: 255–284, 2008.

[3] T. Chan, S. Kang, and J. Shen. Total variation denoising and enhancement of color images based on the CB and HSV color models, *J. Visual Commun. Image Repres.*, 12: 422–435, 2001.

[4] P. Denis, P. Carre, and C. Fernandez-Maloigne. Spatial and spectral quaternionic approaches for colour images, *Comput. Vis. Image Und.*, 107: 74–87, 2007.

[5] Y. Duan, Q. Zhong, X.-C. Tai, and R. Glowinski. A fast operator-splitting method for Beltrami color image denoising, *J. Sci. Comput.*, 92(3): 89, 2022.

[6] J. Duran, M. Moeller, C. Sbert, and D. Cremers. Collaborative total variation: A general framework for vectorial TV models, *SIAM J. Imaging Sci.*, 9: 116–151, 2016.

[7] J. Eckstein and D. Bertsekas. On the Douglas-Rachford splitting method and the proximal point algorithm for maximal monotone operators, *Math. Program.*, 55: 293-318, 1992.

[8] E. Esser. Applications of Lagrangian-Based Alternating Direction Methods and Connections to Split Bregman, *CAM Rep.*, 9, 2009.

[9] H. Y. Fu, M. K. Ng, and J. L. Barlow. Structured total least squares for color image restoration, *SIAM J. Sci. Comput.*, 28(3): 1100–1119, 2006.

[10] H. Y. Fu, M. K. Ng, M. Nikolova, and J. L. Barlow. Efficient minimization methods of mixed l2-l1 and l1-l1 norms for image restoration, *SIAM J. Sci. Comput.*, 27(6): 1881–1902, 2006.

[11] N. P. Galatsanos and A. K. Katsaggelos. Methods for choosing the regularization parameter and estimating the noise variance in image restoration and their relation, *IEEE Trans. Image Process.*, 1(3): 322–336, 1992.

[12] N. P. Galatsanos, A. K. Katsaggelos, R. T. Chin, and A. D. Hillery. Least squares restoration of multichannel images, *IEEE Trans. Signal Process.*, 39: 2222–2236, 1991.

[13] W. R. Hamilton. Elements of Quaternions, *Longmans, Green, and Co, London*, 1866.

[14] P. C. Hansen. Analysis of discrete ill-posed problems by means of the L-curve, *SIAM Rev.*, 34(4): 561–580, 1992.

[15] C. Y. Huang, M. K. Ng, T. T. Wu, and T. Y. Zeng. Quaternion-Based Dictionary Learning and Saturation-Value Total Variation Regularization for Color Image Restoration, *IEEE Trans. Multimedia*, 3769-3781, 2022.

[16] Z. G. Jia. The Eigenvalue Problem of Quaternion Matrix: Structure-Preserving Algorithms and Applications, Beijing, China: *Science Press*, 2019.

[17] Z. G. Jia, Q. Y. Jin, M. K. Ng and X. L. Zhao. Non-local robust quaternion matrix completion for large-scale color image and video inpainting, *IEEE Trans. Image Process.*, 31: 3868–3883, 2022.

[18] Z. G. Jia and M. K. Ng. Structure-preserving quaternion genenralized minimal residual method, *SIAM J. Matrix Anal. A.*, 42(2): 616–634, 2021.

[19] Z. G. Jia, M. K. Ng, and W. Wang. Color image restoration by saturation-value (SV) total variation, *SIAM J. Imaging Sci.*, 12(2): 972–1000, 2019.

[20] Z. G. Jia, M. S. Wei, M. X. Zhao, and Y. Chen. A new real structure-preserving quaternion QR algorithm, *J. Comput. Appl. Math.*, 343: 26–48, 2018.

[21] Y. Jung. Multiple predicting K-fold cross-validation for model selection, *J. Nonparametr Stat.* 30(1): 197–215, 2018.

[22] H. Y. Liao, F. Li, and M. K. Ng. Selection of regularization parameter in total variation image restoration, *JOSA A*, 26(11): 2311–2320, 2011.

[23] H. Liu, X.-C. Tai, R. Kimmel, and R. Glowinski. A color elastica model for vector-valued image regularization, *SIAM J. Imaging Sci.*, 14(2): 717–748, 2021.

[24] H. Liu, X.-C. Tai, R. Kimmel, and R. Glowinski. Elastica models for color image regularization, *SIAM J. Imaging Sci.*, 16(1): 461–500, 2023.

[25] S. Ono and I. Yamada. Decorrelated vectorial total variation, *Proceedings of the IEEE Conference on Computer Vision and Pattern Recognition (CVPR)*, 4090–4097, 2014.

[26] S.-C. Pei and C.-M. Cheng. Novel block truncation coding of image sequences for limited-color display. *ICIAP '97 : Proceedings of the 9th International Conference on Image Analysis and Processing-Volume II*, 164–171, London, U.K.: *Springer-Verlag*, 1997.

[27] F. Pierre, J.-F. Aujol, A. Bugeau, G. Steidl, and V.-T. Ta. Variational contrast enhancement of gray-scale and RGB images, *J. Math. Imaging Vision.*, 57, 99–1168, 2017.

[28] S. J. Sangwine. Fourier transforms of colour images using quaternion or hypercomplex numbers. *Electronics Letters*, 32(21), 1979–1980, October 1996.

[29] G. Sapiro. Vector-valued active contours, *Proc. IEEE Conf. Comput. Vis. Pattern Recog. (CVPR)*, 680–685, 1996.

[30] G. Sharma, W. C. Wu, and E. N. Dalal. The CIEDE2000 color-difference formula: Implementation notes, supplementary test data, and mathematical observations, *Color Res. Appl.*, 30: 21–30, 2005.

[31] W. Wang, L. Pi, and M. K. Ng. Saturation-value total variation model for chromatic aberration correction, *Inverse Probl. Imag.*, 14: 733–755, 2020.

[32] W. Wang and Q. G. Song. Color image restoration based on saturation-value total variation plus L1 fidelity, Inverse Probl., 38(8): 085009, 2022.

[33] W. Wang, Y. M. Yang, and M. K. Ng. A spatial color compensation model using saturation-value total variation, *SIAM J. Imaging Sci.*, 15(3): 1400–1430, 2022.

[34] Z. Wang, A. C. Bovik, H. R. Sheikh, and E. P. Simoncelli. Image quality assessment: from error visibility to structural similarity, *IEEE Trans. Image Process.*, 13(4): 600–612, 2004.

[35] Y. W. Wen and R. H. Chan. Parameter selection for total-variation-based image restoration using discrepancy principle, *IEEE Trans. Image Process.*, 21(4): 1770–1781, 2011.

[36] Y. W. Wen, M. K. Ng, and Y. M. Huang. Efficient total variation minimization methods for color image restoration, *IEEE Trans. Image Process.*, 17(11): 2081–2088, 2008.

[37] J. F. Yang, W. T. Yin, Y. Zhang, Y. L. Wang. A fast algorithm for edge-preserving variational multichannel image restoration, *SIAM J. Imaging Sci.*, 2(2): 569–592, 2009.

[38] J. F. Yang, Y. Zhang, and W. T. Yin. An efficient TVL1 algorithm for deblurring multichannel images corrupted by impulsive noise, *SIAM J. Imaging Sci.*, 31(4): 2842–2865, 2009.

PLACE PHOTO HERE

Zhigang Jia received the Ph.D. degree in mathematics from East China Normal University, Shanghai, China, in 2009. He is currently a Professor in Mathematics, School of Mathematics and Statistics, Jiangsu Normal University, Xuzhou, China. His current research interests include numerical linear algebra, data mining, quaternion matrix computations, color image recognition, medical image processing and imaging science.

PLACE PHOTO HERE

Yuelian Xiang received the M.Sc. degree from Jiangsu Normal University, China, in 2024. She is currently working at Wuhan Vocational College of Software and Engineering, China. Her current research interests include quaternion matrix computation, color image processing, and machine learning.

PLACE PHOTO HERE

Meixiang Zhao received the Ph.D. degree in School of Information and Control Engineering, with a major in control theory and control engineering. Her current research interests include computation intelligence in many-objective optimization, numerical mathematics, machine learning, and applications in face recognition, video processing, big data processing and analysis.

PLACE PHOTO HERE

Tingting Wu received the B.S. and Ph.D. degrees in mathematics from Hunan University, Changsha, China, in 2006 and 2011, respectively. From 2015 to 2018, she was a Postdoctoral Researcher with the School of Mathematical Sciences, Nanjing Normal University, Nanjing, China. She is currently a Professor with the School of Science, Nanjing University of Posts and Telecommunications, Nanjing. Her research interests include variational methods for image processing and computer vision, optimization methods and their applications in sparse recovery, and regularized inverse problems.

PLACE PHOTO HERE

Michael K. Ng received the B.Sc. and M.Phil. degrees from The University of Hong Kong, Hong Kong, in 1990 and 1992, respectively, and the Ph.D. degree from The Chinese University of Hong Kong, Hong Kong, in 1995. From 1995 to 1997, he was a Research Fellow with the Computer Sciences Laboratory, The Australian National University, Canberra, ACT, Australia. He was an Assistant Professor/an Associate Professor with The University of Hong Kong from 1997 to 2005. From 2006 to 2019, he was a Professor/the Chair Professor of the Department of Mathematics, Hong Kong Baptist University, Hong Kong. From 2020 to 2023, he was the Chair Professor of the Research Division of Mathematical and Statistical Science, The University of Hong Kong. He is a Professor/the Chair Professor of the Department of Mathematics, the Dean of Science, Hong Kong Baptist University, Hong Kong. His research interests include bioinformatics, image processing, scientific computing, and data mining. Dr. Ng is selected for the 2017 class of fellows of the Society for Industrial and Applied Mathematics. He received the Feng Kang Prize for his significant contributions to scientific computing. He serves as the editorial board member for several international journals.

APPENDIX

Due to limited pages, we illustrate the solvability of the model and the parameter selection, and present the details of the subproblem of solving CSTV regularization model in this supplementary material.

A. Additional explanation of Figure 3 in the main body

For more clarity, we explain the operational details of Figure 3 in the main body. For the mesh subdivision case, we set the mesh search step to 5×10^{-5}. This searching step is sufficient to explore the superiority of the coupling of the regularization terms without adding additional tuning time. The weighted averaging process for the PSNR and SSIM surfaces is as follows. Firstly, the value ranges of the PSNR and SSIM surfaces are each normalized to the $[0,1]$ interval. Secondly, equal weight factors of 0.5 are assigned to each of the normalized surfaces to achieve the weighted average.

To demonstrate the superiority, we plot the PSNR and SSIM values in Figure 15 at boundary $\lambda_1 = 0$ or $\lambda_2 = 0$. We can see that the PSNR and SSIM values in Figure 15 are significantly smaller than 27.1903 and 0.7704 , respectively.
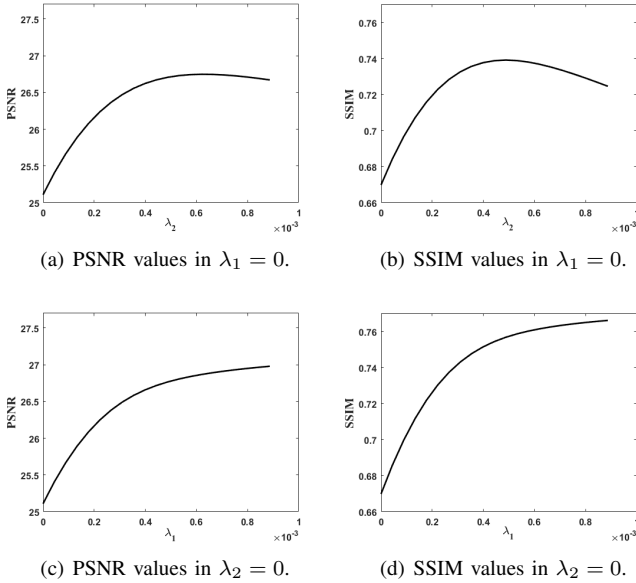

(a) PSNR values in $\lambda_1 = 0$. (b) SSIM values in $\lambda_1 = 0$.

(c) PSNR values in $\lambda_2 = 0$. (d) SSIM values in $\lambda_2 = 0$.

Fig. 15. The values of PSNR and SSIM for the restored image 'statues' in $\lambda_1 = 0$ or $\lambda_2 = 0$.

Proof. The color image cross-channel blurring process is mathematically described as

$$\hat{u}(x,y) = \hat{K} \star u(x,y), \tag{35}$$

where

$$\hat{K} = W \odot K = [K_{ij}\omega_{ij}]_{3\times 3},$$

$$K = \begin{bmatrix} K_{11} & K_{12} & K_{13} \\ K_{21} & K_{22} & K_{23} \\ K_{31} & K_{32} & K_{33} \end{bmatrix}, \quad W = \begin{bmatrix} w_{11} & w_{12} & w_{13} \\ w_{21} & w_{22} & w_{23} \\ w_{31} & w_{32} & w_{33} \end{bmatrix}. \tag{36}$$

That is, $\hat{u}_i(x,y) = \sum_{j=1}^{3} (K_{ij}w_{ij}) \star u_j(x,y)$ for $i = 1, 2, 3$.

Let $u_0(x,y)$ be a zero function. Then the cross-channel blurring process can be embedded into a higher dimentional space,

$$\begin{bmatrix} \hat{u}_0(x,y) \\ \hat{u}_1(x,y) \\ \hat{u}_2(x,y) \\ \hat{u}_3(x,y) \end{bmatrix} = \begin{bmatrix} B_{11} & B_{12} & B_{13} & B_{14} \\ B_{21} & & & \\ B_{31} & & \hat{K} & \\ B_{41} & & & \end{bmatrix} \star \begin{bmatrix} u_0(x,y) \\ u_1(x,y) \\ u_2(x,y) \\ u_3(x,y) \end{bmatrix}, \tag{37}$$

where B_{ij}'s are arbitrary operators of the same size of K_{ij}'s and $\hat{u}_0(x,y) = B_{12}\star u_1(x,y) + B_{1,3}\star u_2(x,y) + B_{14}\star u_3(x,y)$. Denote the extended blurring operator by B, that is,

$$B = \begin{bmatrix} B_{11} & B_{12} & B_{13} & B_{14} \\ B_{21} & & & \\ B_{31} & & \hat{K} & \\ B_{41} & & & \end{bmatrix}. \tag{38}$$

It can be splitted into a sum of a JRS-symmetric operator Q and a 4×4 real block operator R, according to the following rules:

$$B = Q + R, \tag{39}$$

where

$$Q = \frac{1}{4}(B + J_4BJ_4^T + R_4BR_4^T + S_4BS_4^T),$$
$$R = \frac{1}{4}(3B - J_4BJ_4^T - R_4BR_4^T - S_4BS_4^T), \tag{40}$$

and J_4, R_4, S_4 are unitary operators defined in [5]. So we have

$$B \star \begin{bmatrix} u_0(x,y) \\ u_1(x,y) \\ u_2(x,y) \\ u_3(x,y) \end{bmatrix} = Q \star \begin{bmatrix} u_0(x,y) \\ u_1(x,y) \\ u_2(x,y) \\ u_3(x,y) \end{bmatrix} + R \star \begin{bmatrix} u_0(x,y) \\ u_1(x,y) \\ u_2(x,y) \\ u_3(x,y) \end{bmatrix}.$$

Since these unitary operators satisfy $J_4J_4 = -I_{4n}$, $J_4R_4 = S_4$ and $J_4S_4 = -R_4$, we can easily derive

$$J_4QJ_4^T = Q, \quad R_4QR_4^T = Q, \quad S_4QS_4^T = Q.$$

From [5], there exists a quaternion matrix

$$\mathbf{Q} = Q_0 + Q_1\mathbf{i} + Q_2\mathbf{j} + Q_3\mathbf{k} \tag{41}$$

such that

$$Q = \Re(\mathbf{Q}), \tag{42}$$

and

$$Q_0 = \frac{1}{4}(B_{11} + w_{11}K_{11} + w_{22}K_{22} + w_{33}K_{33}),$$
$$Q_1 = \frac{1}{4}(B_{21} - B_{12} + w_{32}K_{32} - w_{23}K_{23}),$$
$$Q_2 = \frac{1}{4}(B_{31} - B_{13} + w_{13}K_{13} - w_{31}K_{31}),$$
$$Q_3 = \frac{1}{4}(B_{41} - B_{14} + w_{21}K_{21} - w_{12}K_{12}). \tag{43}$$

Define $\mathbf{u}(x,y) = u_0(x,y) + u_1(x,y)\mathbf{i} + u_2(x,y)\mathbf{j} + u_3(x,y)\mathbf{k}$ with $u_0(x,y) \equiv 0$. Then

$$\Re_c(\mathbf{u}(x,y)) = [u_0(x,y), u_1(x,y), u_2(x,y), u_3(x,y)]^T.$$

So we have

$$Q \star \Re_c(\mathbf{u}(x,y)) = \Re(\mathbf{Q}) \star \Re_c(\mathbf{u}(x,y)) = \Re_c(\mathbf{Q} \circledast \mathbf{u}(x,y)).$$

Define

$$\begin{bmatrix} r_0(x,y) \\ r_1(x,y) \\ r_2(x,y) \\ r_3(x,y) \end{bmatrix} = R \star \begin{bmatrix} u_0(x,y) \\ u_1(x,y) \\ u_2(x,y) \\ u_3(x,y) \end{bmatrix}$$

and

$$\begin{aligned} \mathbf{r}(x,y) &= \Re_c^{-1}([r_0(x,y), r_1(x,y), r_2(x,y), r_3(x,y)]^T) \\ &= r_0(x,y) + r_1(x,y)\mathbf{i} + r_2(x,y)\mathbf{j} + r_3(x,y)\mathbf{k}. \end{aligned} \quad (44)$$

Then

$$\begin{aligned} B \star \Re_c(\mathbf{u}(x,y)) &= Q \star \Re_c(\mathbf{u}(x,y)) + R \star \Re_c(\mathbf{u}(x,y)) \\ &= \Re(\mathbf{Q}) \star \Re_c(\mathbf{u}(x,y) + \Re_c(\mathbf{r}(x,y)) \quad (45) \\ &= \Re_c(\mathbf{Q} \circledast \mathbf{u}(x,y) + \mathbf{r}(x,y)). \end{aligned}$$

Recall the definition of transformation map $\mathcal{T}$ in the main body that

$$\mathcal{T}(\mathbf{q}(x,y)) := q(x,y) = [q_1(x,y), q_2(x,y), q_3(x,y)]^T \quad (46)$$

for $\mathbf{q}(x,y) = q_0(x,y) + q_1(x,y)\mathbf{i} + q_2(x,y)\mathbf{j} + q_3(x,y)\mathbf{k}$. The blurring process (37) can be rewritten as

$$\hat{u}(x,y) = \hat{K} \star u(x,y) = \mathcal{T}(\mathbf{Q} \circledast \mathbf{u}(x,y) + \mathbf{r}(x,y)), \quad (47)$$

where $\mathbf{Q} = \Re^{-1}(Q)$ and $\mathbf{r}(x,y) = \Re_c^{-1}(R \star \Re_c(\mathbf{u}(x,y)))$.

Moreover, if B_{ij}'s in (43) are set zero operators then we obtain the special quaternion operator $\mathbf{Q}$ in Theorem 1 of the main body. $\square$

In the discrete form, the cross-channel blurring process is in fact a sum of a quaternion matrix-vector product $\mathbf{Qu}$ and a quaternion vector $\mathbf{r}$. The quaternion operations can preserve the ratio of red, green and blue information of color pixels in the blurring process and thus, color confusion and interinfection can be reduced in the deblurring process. As a result, the correlation of color channels are well preserved and the recovered color images can achieve a high quality. In theory, there always exists an invertible quaternion matrix $\mathbf{Q}$ such that $\mathbf{Qu} = \hat{\mathbf{u}}$. However, it is impractical to compute such quaternion matrix, since a large number of pairs of original and observed color images under the same blurring process are in need. Especially, the original color image is definitely unknown. So we alternatively construct $\mathbf{Q}$ according to (41), (43) and (48) to minimize $\|\mathbf{r}\|_2$ in this paper.

The blocks B_{ij}'s of matrix B defined by (38) can be chosen as the solution of the minimization problem:

$$\begin{aligned} \min_{B_{ij}} \quad & \|B - Q\|_F \\ \text{s.t.} \quad & B_{12} \star u_1 + B_{1,3} \star u_2 + B_{14} \star u_3 = 0. \end{aligned} \quad (48)$$

In this way, the quaternion function $\mathbf{r}(x,y)$ in (47) is minimized.

B. The Euler-Lagrange equation of CSTV regularization model

In this section, we derive the Euler-Lagrange equation of CSTV regularization model. Without causing any confusion, we will use $\mathbf{u}(x,y)$ to represent the quaternion function $u_1(x,y)\mathbf{i} + u_2(x,y)\mathbf{j} + u_3(x,y)\mathbf{k}$ or the real vector function $[u_1(x,y), u_2(x,y), u_3(x,y)]^T$ in the following text. Sometimes, (x,y) will ignored for short.

We still explore $p = 2$ as an example in terms of its corresponding Euler-Lagrange equation. The Euler-Lagrange equation corresponding to the function of several variables can be expressed as follows,

$$\frac{\partial f}{\partial u} - \frac{\partial}{\partial x}\frac{\partial f}{\partial_x u} - \frac{\partial}{\partial y}\frac{\partial f}{\partial_y u} = 0. \quad (49)$$

If expressed by the divergence operator, (49) can be equivalently written as

$$\nabla \cdot \left(\frac{\partial f}{\partial_x u} + \frac{\partial f}{\partial_y u}\right) - \frac{\partial f}{\partial u} = 0. \quad (50)$$

To facilitate the representation, give the following notation,

$$\begin{aligned} f_1 &:= \sqrt{(|\partial_x \mathbf{u}(x,y)|_s^2) + (|\partial_y \mathbf{u}(x,y)|_s^2)} \\ &\quad + \alpha\sqrt{(|\partial_x \mathbf{u}(x,y)|_v^2) + (|\partial_y \mathbf{u}(x,y)|_v^2)}, \\ f_2 &:= \sqrt{\sum_{i=1}^{3}(\partial_x u_i(x,y))^2 + (\partial_y u_i(x,y))^2}, \\ f_3 &:= \frac{1}{2}|\hat{K} \star \mathbf{u} - \mathbf{z}|^2. \end{aligned} \quad (51)$$

The Euler-Lagrange equation is constructed with the above notation. Applying the partial derivative to f_1, we have

$$|\partial_x \mathbf{u}|_s^2 = \frac{1}{9}(\partial_x \mathbf{u})^T C^T C (\partial_x \mathbf{u}), \quad (52)$$

and

$$\left(|\partial_x \mathbf{u}|_s^2\right)'_{\partial_x \mathbf{u}} = \frac{1}{9}C^T C (\partial_x \mathbf{u}) = \partial_x(C^2 \mathbf{u}). \quad (53)$$

The above equation can be further simplified as

$$\left(|\partial_x \mathbf{u}|_s^2\right)'_{\partial_x \mathbf{u}} = \frac{1}{3}\partial_x(C\mathbf{u}).$$

A similar result can be obtained for

$$\left(|\partial_y \mathbf{u}|_s^2\right)'_{\partial_y \mathbf{u}} = \frac{1}{3}\partial_y(C\mathbf{u}).$$

For $|\cdot|_v$, we have

$$|\partial_x \mathbf{u}|_v^2 = \frac{1}{3}(\partial_x \mathbf{u})^T(\partial_x \mathbf{u}), \quad (54)$$

and

$$\left(|\partial_x \mathbf{u}|_v^2\right)'_{\partial_x \mathbf{u}} = \frac{1}{3}(\partial_x \mathbf{u}). \quad (55)$$

A similar result can be obtained for

$$\left(|\partial_y \mathbf{u}|_v^2\right)'_{\partial_y \mathbf{u}} = \frac{1}{3}(\partial_y \mathbf{u}).$$

Therefore, for f_1, it holds as follows

$$\begin{aligned} \frac{\partial f_1}{\partial_x \mathbf{u}} &= \frac{1}{3}\left(\frac{\partial_x C\mathbf{u}}{\sqrt{|\partial_x \mathbf{u}|_s^2 + |\partial_y \mathbf{u}|_s^2}} + \frac{\partial_x \mathbf{u}}{\sqrt{|\partial_x \mathbf{u}|_v^2 + |\partial_y \mathbf{u}|_v^2}}\right), \\ \frac{\partial f_1}{\partial_y \mathbf{u}} &= \frac{1}{3}\left(\frac{\partial_y C\mathbf{u}}{\sqrt{|\partial_x \mathbf{u}|_s^2 + |\partial_y \mathbf{u}|_s^2}} + \frac{\partial_y \mathbf{u}}{\sqrt{|\partial_x \mathbf{u}|_v^2 + |\partial_y \mathbf{u}|_v^2}}\right). \end{aligned} \quad (56)$$

In addition, by the definition of f_1 it follows that

$$\frac{\partial f_1}{\partial \mathbf{u}} = 0. \tag{57}$$

Similarly, f_2 and f_3 are calculated: applying the partial derivative to f_2 yields

$$\frac{\partial f_2}{\partial_x \mathbf{u}} = \frac{\partial_x \mathbf{u}}{\|\nabla \mathbf{u}(x,y)\|_2}, \quad \frac{\partial f_2}{\partial_y \mathbf{u}} = \frac{\partial_y \mathbf{u}}{\|\nabla \mathbf{u}(x,y)\|_2}, \quad \frac{\partial f_2}{\partial \mathbf{u}} = 0. \tag{58}$$

Applying the partial derivative to f_3 yields

$$\frac{\partial f_3}{\partial_x \mathbf{u}} = 0, \quad \frac{\partial f_3}{\partial_y \mathbf{u}} = 0, \quad \frac{\partial f_3}{\partial \mathbf{u}} = (\hat{K} \star \mathbf{u} - \mathbf{z}) \star \hat{K}^*, \tag{59}$$

where $\hat{K}^*$ is the conjugate transpose of $\hat{K}$. Combining the above (56), (57), (58), (59), one arrives at the Euler-Lagrange equation in the following form

$$\begin{aligned} &\frac{\lambda_1}{3} \nabla \cdot \left(\frac{\nabla(\mathbf{u}C)}{\sqrt{(|\partial_x \mathbf{u}(x,y)|_s^2) + (|\partial_y \mathbf{u}(x,y)|_s^2)}} \right. \\ &\left. + \alpha \frac{\nabla \mathbf{u}}{\sqrt{(|\partial_x \mathbf{u}(x,y)|_v^2) + (|\partial_y \mathbf{u}(x,y)|_v^2)}} \right) \\ &+ \lambda_2 \frac{\nabla \mathbf{u}}{\|\nabla \mathbf{u}\|_2} - \left(\hat{K} \star \mathbf{u} - \star \mathbf{z} \right) \star \hat{K}^* = 0. \end{aligned} \tag{60}$$

In (60), the proposed model takes into account both the diffusion coefficients of the channel coupling over the saturation and value components and the diffusion coefficients of the summation of the individual channels over the RGB space. The quaternion representation also leads to many other advantages, such as the values of three color channels of a color pixel are flocked together and their physical meanings are preserved in the whole color image processing based on quaternion computation. Especially, color distortion will be hugely reduced in the recovered color image by the new model.

Certainly, both regular terms constrain the gradient information of the image, and in the following the two regularization terms are considered as a whole, so that it is more obvious to see how the CSTV regularization term acts on the gradient. It is sufficient to transform the denominator of the SVTV term. According to the above derivations, the denominator of the SVTV term can be reduced to

$$\begin{aligned} \sqrt{|\partial_x \mathbf{u}|_s^2 + |\partial_y \mathbf{u}|_s^2} &= \frac{1}{3}\sqrt{(\nabla C \mathbf{u})^T (\nabla C \mathbf{u})} = \frac{1}{3}\|\nabla C \mathbf{u}\|_2, \\ \sqrt{|\partial_x \mathbf{u}|_v^2 + |\partial_y \mathbf{u}|_v^2} &= \sqrt{\frac{1}{3}(\nabla \mathbf{u})^T(\nabla \mathbf{u})} = \frac{\sqrt{3}}{3}\|\nabla \mathbf{u}\|_2. \end{aligned} \tag{61}$$

It is interesting to note that, without considering the coefficients, the form of the contribution of the V-component to the gradient in the SVTV is identical to the form of the contribution of the CTV to the gradient. Considering the symmetry of the matrix C, (60) can be rewritten as

$$\begin{aligned} &\nabla \cdot (\lambda_1 \frac{\nabla \frac{C}{3}\mathbf{u}}{\|(\nabla \frac{C}{3}\mathbf{u})\|_2} + (\frac{\sqrt{3}}{3}\alpha\lambda_1 + \lambda_2)\frac{\nabla \mathbf{u}}{\|(\nabla \mathbf{u})\|_2}) \\ &- (\hat{K} \star \mathbf{u} - \mathbf{z}) \star \hat{K}^* = 0. \end{aligned} \tag{62}$$

From equation (62), it is easy to see that the CSTV regularization model can be viewed as a weighted combination of S

and V components in HSV color space to achieve the effect of restoring the color image using both HSV and RGB color space information. This is essentially explained by the fact that the R, G, and B components are all expressed in terms of value, i.e., the V component. Note that it is impractical to solve the Euler-Lagrange equation (62) directly, since a nonlinear differential equation leads to a non-linear system after discretization.

Next, we present the dual form of the CSTV regularization model. The dual forms of regularization functions SVTV and CTV are

$$\text{SVTV}(\mathbf{u}) = \max_{\|g\| \leq 1} \ \langle \text{diag}(1,1,\alpha)\mathbf{P}\mathbf{u}, \nabla g \rangle,$$

$$\text{CTV}(\mathbf{u}) = \max_{\|h\| \leq 1} \ \langle \mathbf{u}, \nabla h \rangle,$$

where $\mathbf{P}$ is an orthogonal transformation matrix that takes the form of

$$\mathbf{P} = \begin{bmatrix} \frac{1}{\sqrt{2}}I & \frac{-1}{\sqrt{2}}I & 0 \\ \frac{1}{\sqrt{6}}I & \frac{1}{\sqrt{6}}I & \frac{-2}{\sqrt{6}}I \\ \frac{1}{\sqrt{3}}I & \frac{1}{\sqrt{3}}I & \frac{1}{\sqrt{3}}I \end{bmatrix}.$$

By converting the regularization terms into dual forms, we can rephrase the CSTV regularization model as the following dual form:

$$\begin{aligned} \min_{\mathbf{u}} \max_{\substack{\|g\| \leq 1 \\ \|h\| \leq 1}} \ &\lambda_1 \langle \text{diag}(1,1,\alpha)\mathbf{P}\mathbf{u}, \nabla g \rangle + \lambda_2 \langle \mathbf{u}, \nabla h \rangle + \\ &\frac{1}{2}\|\mathbf{Q} \circledast \mathbf{u} + \mathbf{r} - \mathbf{z}\|^2. \end{aligned} \tag{63}$$

In the dual form, the solution $\mathbf{u}(x,y)$ can be differentiable or not, which expands the feasible set. Obviously, the min-max problem (63) is a new saddle-point problem.

There are various methods to solve the CSTV regularization model or its dual form (63) with real variables. However, there no methods for solving them with quaternion variables.

C. Augmented Lagrangian method for $(\mathbf{u}, \mathbf{v})$-subproblem

Now, we present a new augmented Lagrangian method for solving $(\mathbf{w}, \mathbf{v})$-subproblem,

$$\begin{aligned} \arg\min_{\mathbf{w},\mathbf{v}} \ &\lambda_1 \text{SVTV}(\mathbf{w}) + \frac{\alpha_1}{2}\|\mathbf{w} - \mathbf{u}\|^2 + \\ &\lambda_2 \text{CTV}(\mathbf{v}) + \frac{\alpha_2}{2}\|\mathbf{v} - \mathbf{u}\|^2. \end{aligned} \tag{64}$$

Since the two variables are independent of each other and have no intersecting terms, we construct the augmented Lagrangian schemes of computing $\mathbf{w}$ and $\mathbf{v}$, respectively.

- $\mathbf{w}$-subproblem
  With $\mathbf{u}$ and $\mathbf{v}$ fixed, the minimization problem (64) is reduced to

$$\arg\min_{\mathbf{w}} \ \lambda_1 \text{SVTV}(\mathbf{w}) + \frac{\alpha_1}{2}\|\mathbf{w} - \mathbf{u}\|^2. \tag{65}$$

We define two discrete differential operators $\mathbf{D}_x$, $\mathbf{D}_y$,

$$\begin{aligned} (\mathbf{D}_x \mathbf{w})_{i,j} &= \mathbf{w}(i,j) - \mathbf{w}(i-1,j), \\ (\mathbf{D}_y \mathbf{w})_{i,j} &= \mathbf{w}(i,j) - \mathbf{w}(i,j-1), \end{aligned}$$

under adequate boundary conditions for color image. Define

$$\mathbf{s} = \mathbf{P}\mathbf{w} \text{ and } \mathbf{q} = \mathbf{P}\mathbf{u}.$$

Then the objective color image restoration model (77) is reformulated as

$$
\arg\min_{\mathbf{s}} \ \frac{\lambda_1}{\alpha_1} \sum_{i=1}^{m} \sum_{j=1}^{n} (\sqrt{\sum_{k=1}^{2}((\mathbf{D}_x s_k)_{ij})^2 + ((\mathbf{D}_y s_k)_{ij})^2}
$$
$$
+ \alpha\sqrt{((\mathbf{D}_x s_3)_{ij})^2 + ((\mathbf{D}_y s_3)_{ij})^2)} + \frac{1}{2}\|\mathbf{s} - \mathbf{q}\|^2. \tag{66}
$$

By introducing auxiliary variables t_i^x and t_i^y, the minimization problem (78) is equivalently rewritten into

$$
\arg\min_{\mathbf{s}} \ \frac{\lambda_1}{\alpha_1} \sum_{i=1}^{m} \sum_{j=1}^{n} (\sqrt{\sum_{k=1}^{2}|(t_k^x)_{ij}|^2 + |(t_k^y)_{ij}|^2}
$$
$$
+ \alpha\sqrt{|(t_3^x)_{ij}|^2 + |(t_3^y)_{ij}^2|)} + \frac{1}{2}\|\mathbf{s} - \mathbf{q}\|^2,
$$
$$
\text{s.t.} \ \ t_1^x = \mathbf{D}_x s_1, t_2^x = \mathbf{D}_x s_2, t_3^x = \mathbf{D}_x s_3,
$$
$$
t_1^y = \mathbf{D}_y s_1, t_2^y = \mathbf{D}_y s_2, t_3^y = \mathbf{D}_y s_3.
$$

The augmented Lagrangian of the aforementioned minimization problem is

$$
\frac{\lambda_1}{\alpha_1} \sum_{i=1}^{m} \sum_{j=1}^{n} (\sqrt{\sum_{k=1}^{2}|(t_k^x)_{ij}|^2 + |(t_k^y)_{ij}|^2}
$$
$$
+ \alpha\sqrt{|(t_3^x)_{ij}|^2 + |(t_3^y)_{ij}^2|)} + \frac{1}{2}\|\mathbf{s} - \mathbf{q}\|^2
$$
$$
+ \sum_{i=1}^{3}((\tau_i^x, t_i^x - \mathbf{D}_x s_i) + (\tau_i^y, t_i^y - \mathbf{D}_y s_i)) \tag{67}
$$
$$
+ \frac{\beta}{2} \sum_{i=1}^{3}(\|t_i^x - \mathbf{D}_x s_i\|^2 + \|t_i^y - \mathbf{D}_y s_i\|^2),
$$

where τ_i^x and τ_i^y are Lagrangian multipliers and β is a positive penalty parameter.

According to the classic framework of the ADMM [2], [3], we construct a method to sovle (67) with three steps as follows.

Step one: When fixing $\mathbf{s}$, t_i^x and t_i^y are computed by using the soft shrinkage functions,

$$
t_i^{x,y} = \max(0, n_1 - \frac{\lambda_1}{\beta\alpha_1}) \cdot \frac{\mathbf{D}_x s_i - \frac{\tau_i^{x,y}}{\beta}}{n_1}, \quad i = 1, 2, \tag{68a}
$$

$$
t_3^{x,y} = \max(0, n_2 - \frac{\alpha\lambda_1}{\beta\alpha_1}) \cdot \frac{\mathbf{D}_x s_3 - \frac{\tau_3^{x,y}}{\beta}}{n_2}, \tag{68b}
$$

where

$$
n_1 = \sqrt{\sum_{i=1}^{2}(\mathbf{D}_x s_i - \frac{\tau_i^x}{\beta})^2 + (\mathbf{D}_y s_i - \frac{\tau_i^y}{\beta})^2},
$$

$$
n_2 = \sqrt{(\mathbf{D}_x s_3 - \frac{\tau_3^x}{\beta})^2 + (\mathbf{D}_y s_3 - \frac{\tau_3^y}{\beta})^2}.
$$

Step two: When fixing t_i^x and t_i^y, $\mathbf{s}$ is computed by solving the following minimization problem

$$
\frac{1}{2}\|\mathbf{s} - \mathbf{q}\|^2 + \sum_{i=1}^{3}((\tau_i^x, t_i^x - \mathbf{D}_x s_i) + (\tau_i^y, t_i^y - \mathbf{D}_y s_i))
$$
$$
+ \frac{\beta}{2} \sum_{i=1}^{3}(\|t_i^x - \mathbf{D}_x s_i\|^2 + \|t_i^y - \mathbf{D}_y s_i\|^2).
$$

The above minimization problem can be equivalently described by the following real linear system

$$
(I + \beta\mathbf{D}_x^T\mathbf{D}_x + \beta\mathbf{D}_y^T\mathbf{D}_y)\mathbf{s}
$$
$$
= \mathbf{q} + \sum_{i=1}^{3}(\mathbf{D}_x^T\tau_i^x + \mathbf{D}_y^T\tau_i^y + \beta\mathbf{D}_x^T t_i^x + \beta\mathbf{D}_y^T t_i^y). \tag{69}
$$

Once $\mathbf{s}$ is computed, we obtain $\mathbf{w} = \mathbf{P}^{-1}\mathbf{s}$.

Step three: The Lagrangian multipliers are updated as follows

$$
\tau_i^x = \tau_i^x + \beta(t_i^x - \mathbf{D}_x s_i), \ \ \tau_i^y = \tau_i^y + \beta(t_i^y - \mathbf{D}_y s_i), \ i = 1, 2, 3.
$$

- **$\mathbf{v}$-subproblem**

  With $\mathbf{u}$ an $\mathbf{w}$ fixed, the minimization problem (64) is reduced to

$$
\arg\min_{\mathbf{v}} \ \lambda_2 \text{CTV}(\mathbf{v}) + \frac{\alpha_2}{2}\|\mathbf{v} - \mathbf{u}\|^2. \tag{70}
$$

We define two discrete differential operators $\mathbf{D}_x$, $\mathbf{D}_y$,

$$
(\mathbf{D}_x\mathbf{v})_{i,j} = \mathbf{v}(i, j) - \mathbf{v}(i - 1, j),
$$
$$
(\mathbf{D}_y\mathbf{v})_{i,j} = \mathbf{v}(i, j) - \mathbf{v}(i, j - 1),
$$

under adequate boundary conditions for color image. Then the objective color image restoration model (82) is reformulated as

$$
\mathbf{v}^* = \arg\min_{\mathbf{v}} \ \frac{\lambda_2}{\alpha_2} \sum_{i=1}^{m} \sum_{j=1}^{n} (\sqrt{\sum_{k=1}^{3}((\mathbf{D}_x v_k)_{ij})^2 + ((\mathbf{D}_y v_k)_{ij})^2}
$$
$$
+ \frac{1}{2}\|\mathbf{v} - \mathbf{u}\|^2. \tag{71}
$$

By introducing auxiliary variables l_i^x and l_i^y, the minimization problem (71) is equivalently rewritten into

$$
\mathbf{v}^* = \arg\min_{\mathbf{v}} \ \frac{\lambda_2}{\alpha_2} \sum_{i=1}^{m} \sum_{j=1}^{n} (\sqrt{\sum_{k=1}^{3}|(l_k^x)_{ij}|^2 + |(l_k^y)_{ij}|^2}
$$
$$
+ \frac{1}{2}\|\mathbf{v} - \mathbf{u}\|^2,
$$
$$
\text{s.t.} \ \ l_1^x = \mathbf{D}_x v_1, l_2^x = \mathbf{D}_x v_2, l_3^x = \mathbf{D}_x v_3,
$$
$$
l_1^y = \mathbf{D}_y v_1, l_2^y = \mathbf{D}_y v_2, l_3^y = \mathbf{D}_y v_3.
$$

The augmented Lagrangian of the aforementioned minimization problem is

$$
\frac{\lambda_2}{\alpha_2}\sum_{i=1}^{m}\sum_{j=1}^{n}(\sqrt{\sum_{k=1}^{3}|(l_k^x)_{ij}|^2+|(l_k^y)_{ij}|^2}+\frac{1}{2}\|\mathbf{v}-\mathbf{u}\|^2
$$
$$
+\sum_{i=1}^{3}((\eta_i^x,l_i^x-\mathbf{D}_x v_i)+(\eta_i^y,l_i^y-\mathbf{D}_y v_i))
$$
$$
+\frac{\beta_2}{2}\sum_{i=1}^{3}(\|l_i^x-\mathbf{D}_x v_i\|^2+\|l_i^y-\mathbf{D}_y v_i\|^2).
$$
(72)

where η_i^x and η_i^y are Lagrangian multipliers and β_2 is a positive penalty parameter. According to the classic framework of the ADMM [2], [3], we construct a method to sovle (72) with three steps as follows. **Step one:** When fixing $\mathbf{v}$, l_i^x and l_i^y are computed by using the soft shrinkage functions,

$$
l_i^{x,y}=\max\left(0,m-\frac{\lambda_2}{\beta_2\alpha_2}\right)\cdot\frac{\mathbf{D}_x v_i-\frac{\eta_i^{x,y}}{\beta_2}}{m},\quad i=1,2,3,
$$
(73)

where

$$
m=\sqrt{\sum_{i=1}^{3}(\mathbf{D}_x v_i-\frac{\eta_i^x}{\beta_2})^2+(\mathbf{D}_y v_i-\frac{\eta_i^y}{\beta_2})^2}.
$$

Step two: When fixing l_i^x and l_i^y, $\mathbf{v}$ is computed by solving the following minimization problem

$$
\frac{1}{2}\|\mathbf{v}-\mathbf{u}\|^2+\sum_{i=1}^{3}((\eta_i^x,l_i^x-\mathbf{D}_x v_i)+(\eta_i^y,l_i^y-\mathbf{D}_y v_i))
$$
$$
+\frac{\beta_2}{2}\sum_{i=1}^{3}(\|l_i^x-\mathbf{D}_x v_i\|^2+\|l_i^y-\mathbf{D}_y v_i\|^2).
$$

The above minimization problem can be equivalently described by the following real linear system

$$
(I+\beta_2\mathbf{D}_x^T\mathbf{D}_x+\beta_2\mathbf{D}_y^T\mathbf{D}_y)\mathbf{v}
$$
$$
=\mathbf{u}+\sum_{i=1}^{3}(\mathbf{D}_x^T\eta_i^x+\mathbf{D}_y^T\eta_i^y+\beta_2\mathbf{D}_x^T l_i^x+\beta_2\mathbf{D}_y^T l_i^y).
$$
(74)

Step three: The Lagrangian multipliers are updated as follows

$$
\eta_i^x=\eta_i^x+\beta_2(l_i^x-\mathbf{D}_x v_i),
$$
$$
\eta_i^y=\eta_i^y+\beta_2(l_i^y-\mathbf{D}_y v_i)\quad(i=1,2,3).
$$

In summary, the $(\mathbf{w},\mathbf{v})$-subproblem needs to compute several soft shrinkage functions and solve two real linear systems.

In this paper, we choose to determine $[\lambda_1,\lambda_2]$ first and subsequently optimize $[\alpha_1,\alpha_2]$ under the determined optimal $[\lambda_1,\lambda_2]$ parameters setting. This parameter selection strategy is formulated based on the following considerations: $[\lambda_1,\lambda_2]$, as the regularization parameters, have more significant impact on the image restoration results. Therefore prioritizing $[\lambda_1,\lambda_2]$ can help stabilize the model performance at an early stage and ensure that the subsequent optimization of $[\alpha_1,\alpha_2]$ parameters can be carried out on a more optimal basis, leading to more accurate restoration results.

Theoretically, the selection of $[\lambda_1,\lambda_2]$ is related to the noise level. In most of numerical experiments, we did not adjust $[\lambda_1,\lambda_2]$ according to changes of noise level, but rather fixed σ at 0.01. The corresponding parameter pairs were initially selected using the L-surface method and then refined through further tuning. This approach effectively reduces the difficulty and time cost of parameter tuning.

If the noise level changes, the optimal $[\lambda_1,\lambda_2]$ parameter pair would also change accordingly. We test this case at the end of Section V-B of the main body. The values of model parameters are given later in Table I of the supplementary material. Adapting the selection of multiple coupled regularization parameters based on the noise level will be a part of our future work.

D. Real algorithms of solving the CSTV regularization model

In this section, we present a real algorithm of solving the CSTV regularization model in the main body, which is denoted by CSTV$_{\text{GMRES}}$.

Following the real ADMM method, we need solve three subproblems alternatively.

- $\mathbf{u}$-subproblem

  Fixing $\mathbf{w}$ and $\mathbf{v}$ simplifies the minimization problem to

$$
\arg\min_{\mathbf{u}}\quad\frac{1}{2}\|\hat{K}\star\mathbf{u}-\mathbf{z}\|^2+\frac{\alpha_1}{2}\|\mathbf{w}-\mathbf{u}\|^2+\frac{\alpha_2}{2}\|\mathbf{v}-\mathbf{u}\|^2.
$$
(75)

  This is essentially a least squares problem, which is the same as solving

$$
(\hat{K}^T\hat{K}+\alpha_1 I+\alpha_2 I)\mathbf{u}=\hat{K}^T\mathbf{z}+\alpha_1\mathbf{w}+\alpha_2\mathbf{v}.
$$
(76)

  In this case $\hat{K}$ is a real matrix, so it can be solved by the general numerical method for the solution of the real linear system. In this paper, we use the real generalized minimal residual method (GMRES), which reduces to the Lanczos method when the coefficient matrix is symmetric [6].

- $\mathbf{w}$-subproblem

  Fixing $\mathbf{u}$ simplifies the minimization problem to

$$
\arg\min_{\mathbf{w}}\quad\frac{\lambda_1}{\alpha_1}\text{SVTV}(\mathbf{w})+\frac{1}{2}\|\mathbf{w}-\mathbf{u}\|^2.
$$
(77)

  We define two discrete differential operators $\mathbf{D}_x$, $\mathbf{D}_y$,

$$
(\mathbf{D}_x\mathbf{w})_{i,j}=\mathbf{w}(i,j)-\mathbf{w}(i-1,j),
$$
$$
(\mathbf{D}_y\mathbf{w})_{i,j}=\mathbf{w}(i,j)-\mathbf{w}(i,j-1).
$$

  Always assume adequate boundary conditions for color image. To better solve the minimization problem (77), the linear transformation $\mathbf{P}$ is applied to $\mathbf{w}$, and

$$
\mathbf{s}=\left[\begin{array}{ccc}s_1,s_2,s_3\end{array}\right]^T=\mathbf{P}\left[\begin{array}{ccc}w_r,w_g,w_b\end{array}\right]^T.
$$

  Without failing the general, we set $\mathbf{q}=\mathbf{P}\mathbf{u}$. Then the objective color image restoration model (77) is reformulated as

$$
\mathbf{s}^*=\arg\min_{\mathbf{s}}\quad\frac{\lambda_1}{\alpha_1}\sum_{i=1}^{m}\sum_{j=1}^{n}(\sqrt{\sum_{k=1}^{2}((\mathbf{D}_x s_k)_{ij})^2+((\mathbf{D}_y s_k)_{ij})^2}
$$
$$
+\alpha\sqrt{((\mathbf{D}_x s_3)_{ij})^2+((\mathbf{D}_y s_3)_{ij})^2})+\frac{1}{2}\|\mathbf{s}-\mathbf{q}\|^2.
$$
(78)

By introducing auxiliary variables, the minimization problem (78) can be rewritten as an equivalent minimization problem,

$$
\begin{aligned}
\mathbf{s}^* = \arg\min_{\mathbf{s}} \ & \frac{\lambda_1}{\alpha_1} \sum_{i=1}^m \sum_{j=1}^n \left(\sqrt{\sum_{k=1}^2 |(t_k^x)_{ij}|^2 + |(t_k^y)_{ij}|^2} \right. \\
& + \left. \alpha \sqrt{|(t_3^x)_{ij}|^2 + |(t_3^y)_{ij}^2|} \right) + \frac{1}{2}\|\mathbf{s}-\mathbf{q}\|^2, \\
\text{s.t.} \ & t_1^x = \mathbf{D}_x s_1, t_2^x = \mathbf{D}_x s_2, t_3^x = \mathbf{D}_x s_3, \\
& t_1^y = \mathbf{D}_y s_1, t_2^y = \mathbf{D}_y s_2, t_3^y = \mathbf{D}_y s_3.
\end{aligned}
$$

The augmented Lagrangian of the aforementioned minimization problem is as follows after introducing Lagrangian multipliers τ_i^x, τ_i^y ($i=1,2,3$) and the positive penalty parameter β,

$$
\begin{aligned}
& \frac{\lambda_1}{\alpha_1} \sum_{i=1}^m \sum_{j=1}^n \left(\sqrt{\sum_{k=1}^2 |(t_k^x)_{ij}|^2 + |(t_k^y)_{ij}|^2} \right. \\
& + \left. \alpha\sqrt{|(t_3^x)_{ij}|^2 + |(t_3^y)_{ij}^2|} \right) + \frac{1}{2}\|\mathbf{s}-\mathbf{q}\|^2 \\
& + \sum_{i=1}^3 ((\tau_i^x, t_i^x - \mathbf{D}_x s_i) + (\tau_i^y, t_i^y - \mathbf{D}_y s_i)) \\
& + \frac{\beta}{2} \sum_{i=1}^3 (\|t_i^x - \mathbf{D}_x s_i\|^2 + \|t_i^y - \mathbf{D}_y s_i\|^2).
\end{aligned} \quad (79)
$$

The minimum score of (79) can be achieved by using the classic framework of the ADMM [2], [3].

When fixing $\mathbf{s}$, the solutions are giving by using the soft shrinkage algorithm,

$$
t_i^{x,y} = \max\left(0, n_1 - \frac{\lambda_1}{\beta\alpha_1}\right) \cdot \frac{\mathbf{D}_x s_i - \frac{\tau_i^{x,y}}{\beta}}{n_1}, \quad i=1,2, \tag{80a}
$$

$$
t_3^{x,y} = \max\left(0, n_2 - \frac{\alpha\lambda_1}{\beta\alpha_1}\right) \cdot \frac{\mathbf{D}_x s_3 - \frac{\tau_3^{x,y}}{\beta}}{n_2}, \tag{80b}
$$

where

$$
n_1 = \sqrt{\sum_{i=1}^2 (\mathbf{D}_x s_i - \frac{\tau_i^x}{\beta})^2 + (\mathbf{D}_y s_i - \frac{\tau_i^y}{\beta})^2},
$$

$$
n_2 = \sqrt{(\mathbf{D}_x s_3 - \frac{\tau_3^x}{\beta})^2 + (\mathbf{D}_y s_3 - \frac{\tau_3^y}{\beta})^2}.
$$

When fixing t_i^x, t_i^y, the minimization problem is reduced to

$$
\begin{aligned}
& \frac{1}{2}\|\mathbf{s}-\mathbf{q}\|^2 + \sum_{i=1}^3 ((\tau_i^x, t_i^x - \mathbf{D}_x s_i) + (\tau_i^y, t_i^y - \mathbf{D}_y s_i)) \\
& + \frac{\beta}{2} \sum_{i=1}^3 (\|t_i^x - \mathbf{D}_x s_i\|^2 + \|t_i^y - \mathbf{D}_y s_i\|^2).
\end{aligned}
$$

Then, the above minimization problem can be equivalently described by the following real linear system

$$
\begin{aligned}
& (I + \beta \mathbf{D}_x^T \mathbf{D}_x + \beta \mathbf{D}_y^T \mathbf{D}_y)\mathbf{s} \\
& = \mathbf{q} + \sum_{i=1}^3 (\mathbf{D}_x^T \tau_i^x + \mathbf{D}_y^T \tau_i^y + \beta \mathbf{D}_x^T t_i^x + \beta \mathbf{D}_y^T t_i^y).
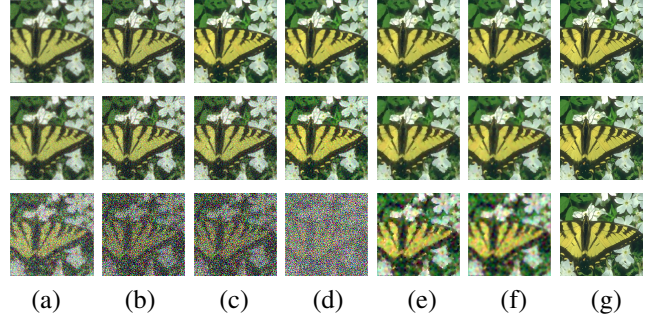\end{aligned} \quad (81)
$$

Fig. 16. Visual comparison of five methods in asymmetric cross-channel deblurring corresponding to the numerical results in Table III of Section V-B in the main body. From left to right: (a) Observed color images, (b) Restorations of CTV_1, (c) Restorations of CTV_2, (d) Restorations of MTV, (e) Restorations of SVTV, (f) Restorations of CSTV, (g) Original color images. From up to down, the noise levels are 0.05, 0.1 and 0.5.

The new value of $\mathbf{w}$, after satisfying the stopping criteria and exiting the iteration, is $\mathbf{P}^{-1}\mathbf{s}$.

The laws for updating the Lagrangian multipliers are as follows

$$
\tau_i^x = \tau_i^x + \beta(t_i^x - \mathbf{D}_x s_i), \ \ \tau_i^y = \tau_i^y + \beta(t_i^y - \mathbf{D}_y s_i)(i=1,2,3).
$$

- **v**-subproblem

Fixing $\mathbf{u}$ allows $\mathbf{v}$ to be refreshed at the same time.

$$
\arg\min_{\mathbf{v}} \ \frac{\lambda_2}{\alpha_2}\text{CTV}(\mathbf{v}) + \frac{1}{2}\|\mathbf{v}-\mathbf{u}\|^2. \tag{82}
$$

The solution to the minimization problem (82) is given by [1]. To obtain the minimum value point, this can also be solved by using a method similar to that of the **w**-subproblem.

E. Numerical results for color image debluring with different levels of noise

In Figure 16, we present the visual comparison of the compared methods: CTV_1, CTV_2, MTV, SVTV and CSTV in the Section V-B of the main body.

In Table V, we present the optimal values of parameters of the compared methods corresponding to the numerical results in Table III of Section V-B in the main body.

TABLE V
OPTIMAL VALUES OF PARAMETERS OF THE COMPARED METHODS
CORRESPONDING TO THE NUMERICAL RESULTS IN TABLE III OF SECTION
V-B IN THE MAIN BODY

Noise level	Method	λ_1	α_1	λ_2	α_2
0.05	CTV_1	0.1000	-	-	-
	CTV_2	0.0161	-	-	-
	MTV	0.0100	-	-	-
	SVTV	0.0443	0.1259	-	-
	CSTV	0.0398	0.1259	0.0028	0.1259
0.1	CTV_1	0.1000	-	-	-
	CTV_2	0.0167	-	-	-
	MTV	0.0100	-	-	-
	SVTV	0.1197	0.2826	-	-
	CSTV	0.1330	0.2827	0.0027	0.0426
0.5	CTV_1	0.0909	-	-	-
	CTV_2	0.0123	-	-	-
	MTV	0.0100	-	-	-
	SVTV	0.7094	0.2821	-	-
	CSTV	0.6651	0.2821	0.01995	0.0300

In Table VI, we present the numbers of iteration steps of the compared methods corresponding to the setting in Section V-B in the main body.

TABLE VI
NUMBERS OF ITERATION STEPS OF THE COMPARED METHOD IN COLOR IMAGE DEBLURRING WITHOUT NOISE

Method	Outer	Inner for $\mathbf{u}$	Inner for $\mathbf{w}$	Inner for $\mathbf{v}$
CTV_1	3	-	-	-
CTV_2	3	-	-	-
MTV	35	-	-	-
SVTV	21	1	5	-
CSTV	34	3	5	5

F. Injective assumption

The requirement in Theorem 2 of the main body that the mapping $\mathbf{u} \mapsto \mathbf{Q} \circledast \mathbf{u} + \mathbf{r}$ is injective is motivated by a general assumption for blurring problems. Whether or not mapping $\mathbf{u} \mapsto \mathbf{Q} \circledast \mathbf{u} + \mathbf{r}$ is injective is related to whether or not the matrix corresponding to the cross-channel blurring operator $\hat{K}$ is nonsingular. It would be sufficient to show that $u \mapsto \hat{K} \star u$ is injective: if $\hat{K} \star u^a = \hat{K} \star u^b$, then $u^a = u^b$. And under known conditions:

$$\hat{K} \star \begin{bmatrix} u_1^a - u_1^b \\ u_2^a - u_2^b \\ u_3^a - u_3^b \end{bmatrix} = 0.$$

The requirement that the above linear system has only 0 solutions means that the matrix corresponding to $\hat{K}$ is required to be nonsingular.

G. HSV color space and quaternion representation

Although the geometry of HSV color space is different from RGB color space, HSV color space can be represented using quaternion operations. Representing a color image pixel as a pure imaginary quaternion, for any position (x, y) in the image domain Ω we have

$$\mathbf{u}(x, y) = u_1(x, y)\mathbf{i} + u_2(x, y)\mathbf{j} + u_3(x, y)\mathbf{k}.$$

With the above representation, the components in the HSV color space can be represented as

$$c_h(x, y) = \tan^{-1}\left(\frac{|\mathbf{u}(x, y) - \boldsymbol{\mu}\boldsymbol{\nu}\mathbf{u}(x, y)\boldsymbol{\nu}\boldsymbol{\mu}|}{\mathbf{u}(x, y) - \boldsymbol{\nu}\mathbf{u}(x, y)\boldsymbol{\nu}}\right),$$

$$c_s(x, y) = \frac{1}{2}|\mathbf{u}(x, y) + \boldsymbol{\mu}\mathbf{u}(x, y)\boldsymbol{\mu}|,$$

$$c_v(x, y) = \frac{1}{2}|\mathbf{u}(x, y) - \boldsymbol{\mu}\mathbf{u}(x, y)\boldsymbol{\mu}|,$$

where $\boldsymbol{\mu} = (\mathbf{i} + \mathbf{j} + \mathbf{k})/\sqrt{3}$ referring to the grey-value axis, and $\boldsymbol{\nu}$ is a unit and pure quaternio number and $\boldsymbol{\nu}$ is orthogonal to $\boldsymbol{\mu}$. With the matrix C defined in [4], we can explicitly represent the S-component and V-component of HSV with u_r, u_g, u_b. We have described the specifics on page 3 of the main body. On the other hand, we consider combining the advantages of RGB and HSV spaces to improve image processing. The quaternion can be used as a unified framework to integrate information from different color spaces to enhance image restoration.

H. The dual form of SVTV regularization

The dual form of the SVTV regularization is provided in [4], along with a summary of the SVTV regularization's convexity, lower semi-continuity, approximation, and compactness characteristics. These characteristics are informative in demonstrating the existence of the model solution put out in this work. In [4], an image recovery model is constructed using the SVTV regularization described above, and the Euler–Lagrange equation of this model is given in terms of Gradient Descent Flow:

$$\nabla \cdot \left(\frac{\nabla (2u_{c_1} - u_{c_2} - u_{c_3})}{\sqrt{(|\partial_x \mathbf{u}(x, y)|_s^2) + (|\partial_y \mathbf{u}(x, y)|_s^2)}} \right.$$
$$\left. + \alpha \frac{\nabla (u_r + u_g + u_b)}{\sqrt{(|\partial_x \mathbf{u}(x, y)|_v^2) + (|\partial_y \mathbf{u}(x, y)|_v^2)}} \right)$$
$$- 3\lambda \left(\hat{K} \star u_{c_1} - z_{c_1} \right) \star \hat{K}^* = 0,$$

where c_1, c_2, c_3 is a sort of cyclic arrangement of r, g, b (There are three arrangements in total: $r, g, b; g, b, r; b, r, g$). It can be seen from these equations that each channel is not calculated independently. Rather, the three channels are coupled together and the information from all three channels is used simultaneously, which ensures the effectiveness of the cross-channel deblurring model proposed later.

We refer to [4] for the details of transform from quaternion functional to real one.

The quaternion blur operator $\mathbf{Q}$ in Definition 2 of the main body depicts the rendering between color channels. Its working principle is shown in Figure 17.
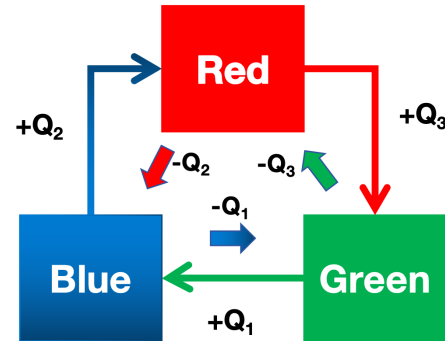

Fig. 17. Working principle of $\mathbf{Q}$.

REFERENCES

[1] X. Bresson and T. Chan. Fast dual minimization of the vectorial total variation norm and applications to color image processing, *Inverse Probl. Imag.*, 2: 255–284, 2008.

[2] J. Eckstein and D. Bertsekas. On the Douglas-Rachford splitting method and the proximal point algorithm for maximal monotone operators, *Math. Program.*, 55: 293-318, 1992.

[3] E. Esser. Applications of Lagrangian-Based Alternating Direction Methods and Connections to Split Bregman, *CAM Rep.*, 9, 2009.

[4] Z. G. Jia, M.K. Ng, and W. Wang. Color Image Restoration by Saturation-Value (SV) Total Variation, *SIAM J. Imaging Sci.*, 12(2): 972–1000, 2019.

[5] Z. G. Jia, M. S. Wei, M. X. Zhao, and Y. Chen. A new real structure-preserving quaternion QR algorithm, *J. Comput. Appl. Math.*, 343: 26–48, 2018.

[6] Y. Saad. Iterative Methods for Sparse Linear Systems, SIAM, Philadelphia, 2003.